#### **ARTICLE**



# Fluid-rock sulfidation reactions control Au-Ag-Te-Bi precipitation in the Val-d'Or orogenic gold vein field (Abitibi subprovince, Canada)

Michael Herzog<sup>1</sup> · Crystal LaFlamme<sup>1,2</sup> · Georges Beaudoin<sup>1</sup> · Guillaume Barré<sup>1</sup> · Laure Martin<sup>2</sup> · Dany Savard<sup>3</sup>

Received: 7 August 2023 / Accepted: 17 January 2024 / Published online: 10 February 2024 © The Author(s), under exclusive licence to Springer-Verlag GmbH Germany, part of Springer Nature 2024

#### Abstract

The Val-d'Or vein field (VVF), located in the southern Abitibi subprovince (Québec, Canada), is host to ~47 Moz gold and is therefore an example of a greenstone-hosted orogenic gold district. Gold is contained in quartz-tourmaline-carbonate veins that cut As-poor intermediate to mafic volcanic and intrusive rocks, including dioritic, granodioritic and gabbroic sills. dikes, stocks, and plutons. Five investigated orebodies (Goldex, Triangle, Plug #4, Pascalis Gold Trend, Beaufor) host gold in vein- and wallrock-hosted pyrite-rich sulfide aggregates (>95 vol%) that show a porous core domain (Py1), with abundant inclusions of carbonate, silicate, and Fe-oxides up to several tens of µm in size. A homogeneous pyrite rim domain (Py2) surrounds Pv1 and contains most of the gold as native gold and polymetallic (Au-Ag-Te-Bi) inclusions, primarily calaverite and petzite. The two pyrites show different Au and As contents (Py1 = Au  $\leq$  30 ppm; As  $\leq$  67 ppm; Py2 = Au  $\leq$  1250 ppm; As  $\leq$  550 ppm). Pyrite shows a ubiquitous shift in  $\delta^{34}$ S values of up to +3.0% from Py1 ( $\delta^{34}$ S = -0.4% to 5.8%, n=32) to Py2 ( $\delta^{34}$ S = 0.0% to 6.3%, n = 59) and records a small, slightly negative  $\Delta^{33}$ S signature between – 0.20% and 0.01%. The  $\delta^{34}$ S shift suggests that removal of reduced sulfur species from auriferous hydrothermal fluids causes the formation of inclusion-hosted gold in Py2 by a decrease in the fluid sulfur fugacity (fS2) through wallrock sulfidation of Fe-oxides. The shift also correlates with locally enriched Co and Ni concentrations in Py1 (<1 wt%), compared to lower, oscillatory zoned concentrations (<0.1 wt%) in Py2, respectively, indicating an overall decrease in fluid oxygen fugacity ( $fO_2$ ). Contemporaneously, a decrease in fluid tellurium fugacity (fTe<sub>2</sub>) drives polymetallic inclusion-hosted gold formation in Py2, initially as calaverite followed by increasingly Ag-bearing petzite and hessite. The multiple sulfur isotopes and trace element compositions recorded in pyrite in the VVF indicate that a homogeneous fluid reservoir introduced gold-sulfide complexes. Even if considered a localized process at the ore-shoot scale, fluid-wallrock sulfidation reactions can lead to a coupled decrease in  $fS_2$ ,  $fO_2$ , and  $fTe_2$  of auriferous hydrothermal fluids in a greenstone-hosted As-poor gold district.

Keywords Archean · Orogenic gold · Multiple sulfur isotopes · Sulfide trace elements · Abitibi subprovince

Editorial handling: M. Fayek

- Michael Herzog michael.herzog.1@ulaval.ca
- Département de Géologie et de Génie Géologique, Faculté des Sciences et de Génie, Université Laval, 1065 Av. de la Médicine, Québec City, Québec G1V 0A6, Canada
- <sup>2</sup> Centre for Microscopy, Characterisation & Analysis, University of Western Australia, 35 Stirling Highway, Perth, WA 6009, Australia
- <sup>3</sup> Laboratoire des Matériaux Terrestres, Université du Québec à Chicoutimi, 555 Boulevard de L'Université, Chicoutimi, Québec G7H 2B1, Canada

# Introduction

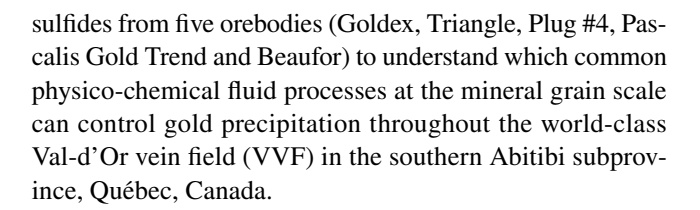
Orogenic gold mineralization accounts for more than 6573 Moz of Au, or 41% of historic global gold production, and is widely accepted to occur along high-angle reverse shear zones that channel fluids by repeated fault-valve processes during cyclic supralithostatic fluid pressure fluctuations (Sibson et al. 1988; Sibson and Scott 1998; Lipson 2014; Cox 2016). These brittle-ductile shear zones develop primarily in the middle to upper crust during compressional periods, and quartz-carbonate veins commonly form along the retrograde path of an orogenic cycle, and post-date peak metamorphic conditions by up to 80 million years (Groves 1993, 2003; Groves et al. 2005; Condie 2000; Kerrich et al. 2000; Goldfarb et al. 2001, 2005; Bierlein



et al. 2006; Groves and Santosh 2016; Herzog et al. 2023). Hydrothermal events associated with an orogenic cycle have the potential to release metamorphic and/or magmatic fluids that accumulate at < 10 km depth, below the brittleductile transition. At the gold precipitation site, key fluid mechanisms such as pressure variations, fluid mixing, or fluid-wallrock reactions have been considered main drivers to cause orogenic gold formation (Phillips 1986; Colvine 1989; Hodgson and Hamilton 1989; Hodgson 1993; Robert 1997; Robert et al. 2005; Ward et al. 2017; Sugiono et al. 2022). Many orogenic gold deposits are hosted in meta-sedimentary rocks. In such cases, gold is commonly hosted by As-rich pyrite (>>1 wt%) and/or arsenopyrite. An increase in As leads to efficient lattice-bound gold deposition in Asrich pyrite through coupled Au-As redox reactions (Reich et al. 2005; Pitcairn et al. 2006; Pokrovski et al. 2019, 2021; McDivitt et al. 2022; Sugiono et al. 2022). In contrast, many greenstone gold districts are dominated by As-poor mafic volcanic rocks, such as in the Xiaoqinling district (North China Craton), Mt Pleasant district (Yilgarn Craton), Timmins-Porcupine (Superior Craton), or Hope Bay belt (Slave Craton), indicating that As is not a requirement for orogenic gold formation (Bi et al. 2011; Sherlock et al. 2012; LaFlamme et al. 2018b; Dubé and Mercier-Langevin 2020; Dubé et al. 2020). This implies that physico-chemical processes, which occur during crustal fluid advection in Aspoor mafic volcanic and sedimentary rocks and that lead to highly localized sulfide and gold precipitation in veins, remain to be fully understood at the sulfide grain scale.

Based on a detailed paragenetic sequence, in situ microanalytical techniques have the potential to elucidate physicochemical processes that result in the precipitation of gold and gold-bearing sulfides. Changes in fluid chemistry leading to gold precipitation may be constrained based on textural observations in combination with high-resolution multiple S isotope and trace element composition of gold-hosting sulfides (e.g., LaFlamme et al. 2018c; Sugiono et al. 2022). Two physico-chemical parameters have a strong effect on Au solubility: the fluid sulfur  $(fS_2)$  and oxygen  $(fO_2)$  fugacities. Changes in  $fS_2$  and  $fO_2$  of a hydrothermal fluid influence the  $\delta^{34}$ S signature, the minor and trace element composition, including gold-bisulfide complex solubility (Pokrovski et al. 2014, 2015, 2022), precipitated sulfides and associated phases (e.g., Sugiono et al. 2022). Other important parameters to monitor local physico-chemical processes include variations of Co and Ni concentrations, which show both an increased solubility at higher fO2 conditions and can provide additional information on fO2 fluctuations at the time of sulfide deposition (Peterson and Mavrogenes 2014; Fougerouse et al. 2016; Ward et al. 2017; Daver et al. 2020; Jansson and Liu 2020; Sugiono et al. 2022).

In this study, we present textural evidence, multiple sulfur isotopes, and trace element compositions of Au-bearing



# Regional geological setting

The southeastern margin of the Superior Craton (Fig. 1a) comprises two subprovinces, the Abitibi and the Pontiac, that are structurally juxtaposed along the Larder Lake-Cadillac fault zone (LLCfz; Fig. 1b). The Abitibi subprovince comprises greenstone belts consisting of volcano-sedimentary rocks intruded by granitic plutons and, in general, metamorphosed to the sub-greenschist and locally up to amphibolite facies. The ultramafic, mafic, and felsic submarine volcanic sequences were deposited between ca. 2795 and 2695 Ma, and the volcanic successions were intruded by plutons of tonalitic, granodioritic, dioritic, and monzonitic compositions between ca. 2750 and 2630 Ma (Latulippe 1966; Pyke et al. 1973; Dimroth et al. 1978, 1983; Hyde 1980; Scott et al. 2002; Ross et al. 2011a, b; Dubé and Mercier-Langevin 2020). The Pontiac subprovince structurally underlies the Abitibi subprovince to the north (Fig. 1b) and consists of sedimentary rocks of the Pontiac Group metamorphosed from upper greenschist to amphibolite facies. The Pontiac Group is composed of turbiditic graywacke and mudstones with lesser ultramafic-mafic volcanic and compositionally varied intrusive rocks (Camiré et al. 1993; Thurston et al. 2008; Piette-Lauzière et al. 2019; Rehm et al. 2021). The Abitibi-Wawa Orogeny affected the two subprovinces throughout a prolonged period of ~ 120 million years from ca. 2700 Ma to 2580 Ma and caused thick-skinned and thin-skinned tectonics with several compressive periods between ≤ 2685 and ≥ 2640 Ma (Moser 1994; Mercier-Langevin et al. 2007; Thurston et al. 2008; Dubé and Mercier-Langevin 2020). Both subprovinces were affected by contemporaneous low- to medium-grade regional metamorphism between ca.  $\leq 2669$  and  $\geq 2643$  Ma and  $\leq 2665$  and 2645 Ma (Machado et al. 1991; Davis et al. 1994; Powell et al. 1995; Piette-Lauzière et al. 2019).

# Geological setting of the Val-d'Or vein field

The stratigraphic sequence that hosts the VVF (Fig. 1b) comprises the Malartic and Louvicourt groups (Fig. 2). The oldest unit of the Malartic Group is the La Motte-Vassan Formation (2714 $\pm$ 2 Ma), which comprises effusive ultramafic, komatiitic rocks. The overlying Dubuisson Formation (2708 $\pm$ 2 Ma) is characterized by ultramafic–mafic



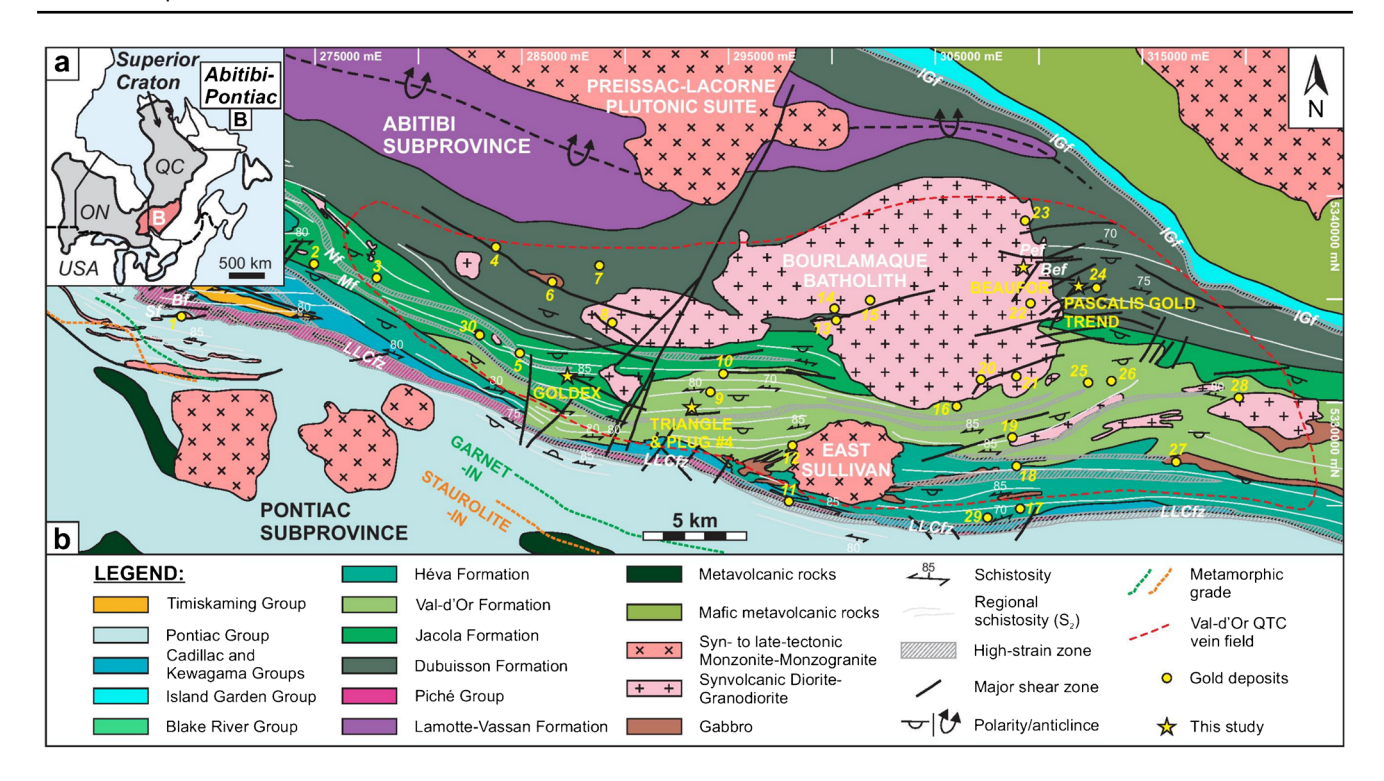


**Fig. 1** a Map outlining the extent of the Superior Craton and location of the Abitibi and Pontiac subprovinces. **b** Geological map of the area between Malartic and Val-d'Or showing the outline of the Val-d'Or vein field, as well as the studied and other gold deposits (after Wong et al. 1991; Morasse et al. 1995; Pilote et al. 2000; Bedeaux et al. 2017; Montsion et al. 2018; SIGÉOM 2020). Bf=Barnat fault, IGf=Island Garden fault, MF=Marbenite fault, Nf=Norbenite fault, QTC=quartz-tourmaline-carbonate, Sf=Sladen

fault. 1=Canadian Malartic, 2=Camflo, 3=Norlartic, 4=Wesdome, 5=Shawkey, 6=Siscoe, 7=Siscoe Extension, 8=Sullivan, 9=Lamaque, 10=Sigma, 11=Orenada Zone 4, 12=East Sullivan, 13=Bras d'Or, 14=New Formaque, 15=Lac Herbin, 16=Manitou-Barvue, 17=Akasaba, 18=Louvicourt Goldfield, 19=Dunraine, 20=Wrightbar, 21=Beacon 2, 22=Courvan, 23=Pascalis North, 24=Lucien C. Béliveau, 25=Louvem, 26=Louvicourt, 27=Sigma 2, 28=Bevcon, 29=Akasaba West, 30=Kiena

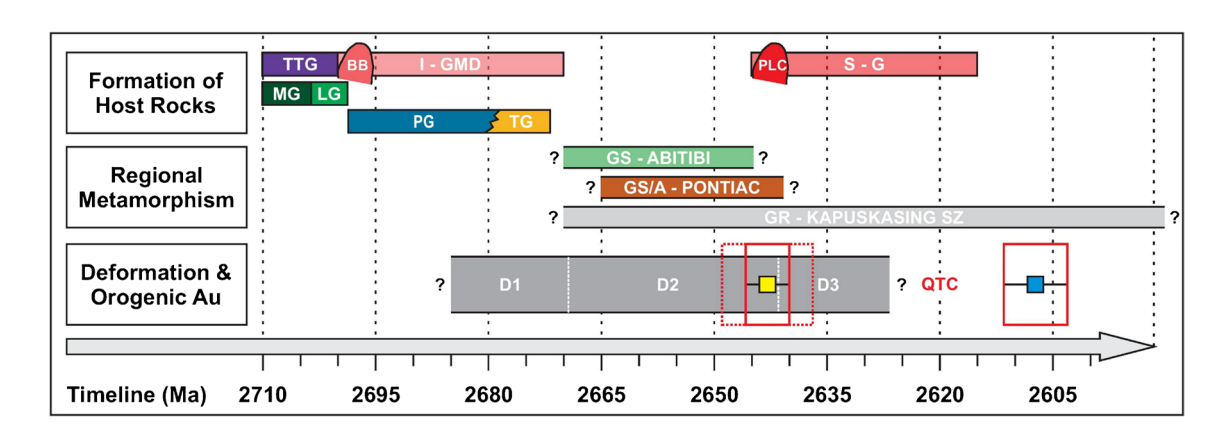


**Fig. 2** Simplified timeline reflecting the temporal and structural framework of the Malartic-Val-d'Or district, highlighting the major period of orogenic gold mineralization commonly inferred based on cross-cutting relationships of dikes with faults, shears, fabrics, and structural data in the VVF (c.f. Ayer et al. 2005; Dubé and Gosselin 2007; Bedeaux et al. 2017). In situ analyses of QTC veins (Herzog et al. 2023) define one period of gold deposition and a later period of hydrothermal fluid flow that remobilized gold. A=amphibolite

facies metamorphism, BB=Bourlamaque batholith, GR=granulite facies metamorphism, GS=greenschist facies metamorphism, I-GMD=I-type granodiorite-monzonite-diorite, KSZ=Kapuskasing Structural Zone, LG=Louvicourt Group, MG=Malartic Group, PG=Pontiac Group, PLC=Preissac-LaCorne Plutonic Suite, QTC=quartz-tourmaline-carbonate, S-G=S-type granite, TTG=tonalite-trondhjemite-granodiorite



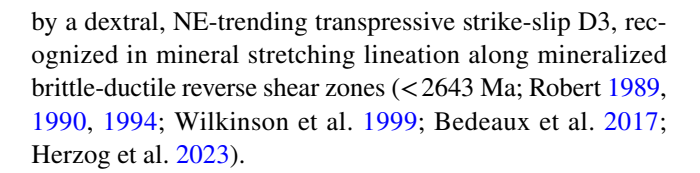
rocks with local felsic rocks (Pilote et al. 2000, 2015). The youngest unit of the Malartic Group, the Jacola Formation (2706±2 Ma), contains mafic volcanic rocks, such as pillow basalts (Machado and Gariépy 1994). The oldest unit of the Louvicourt Group is the Val-d'Or Formation (2704±1 Ma), composed of basaltic pillow lavas and pyroclastic andesitic rocks. The youngest rocks of the Louvicourt Group are the volcaniclastic mafic to felsic rocks of the Héva Formation (2702±2 Ma; Machado and Gariépy 1994; Pilote et al. 2000, 2015).

# Tectono-magmatic history of the Val-d'Or vein field

The VVF (Fig. 2) is the result of two major magmatic, two compressive and one transpressive periods during the Abitibi-Wawa Orogeny, which caused regional large-scale folds and fabrics observed (Moser 1994).

A first period of I-type plutonism (Fig. 2) included the  $2699.8 \pm 1.0$  Ma syn-volcanic Bourlamaque batholith, a quartz-granodiorite-diorite (Wong et al. 1991). Near contemporaneous small-scale intrusions include the gabbroic  $2693.2 \pm 4.7$  Ma Plug #4 (Dubé 2018), the  $2687 \pm 1.2$  Ma sill-like Goldex quartz-diorite to granodiorite (David 2019; Munger 2019), the  $2685 \pm 0.9$  Ma Triangle diorite (Dubé 2018), and the  $2684 \pm 1$  Ma East Sullivan monzonite stock (Pilote et al. 1999). Between 2645 and 2613 Ma, a second S-type intrusive period generated the Preissac-LaCorne plutonic suite, located northeast of Val-d'Or (Feng et al. 1992; Kerrich and King 1993; Chown et al. 2002; Davis 2021).

The earliest compressive period D1 (ca. 2685–2669 Ma) is inferred in the Malartic-Val'd-Or district by large-scale folding (F1) and formed structural corridors that are subparallel to the LLCfz (Imreh 1984; Corfu 1993; Morasse et al. 1995; Morasse 1998; Dubé and Mercier-Langevin 2020). These F1 folds are only locally observed further in the west in the areas of Rouyn-Noranda (Poulsen 2017) and Timmins (Ferguson et al. 1968; Bleeker 2015), lack axial planar foliation, and are truncated by the Timiskaming unconformity. The second compressive period D2 is the result of N-S shortening that superimposed the regional penetrative foliation (S2) on volcanic bedding (Robert 1989, 1990; Corfu et al. 1991; Bedeaux et al. 2017; De Souza et al. 2017; Dubé and Mercier-Langevin 2020). East trending sub-vertical and steeply N-dipping F2 folds and S2 axial planar foliation (Fig. 1b) strongly affect the Timiskaming Group, constraining the maximum age for D2 at  $\leq$  2669 Ma (Dimroth et al. 1983; Daigneault et al. 2002; Robert et al. 2005; Bleeker 2015). Pegmatitic dikes associated with the Preissac-LaCorne plutonic suite at ca. 2647 Ma (Feng and Kerrich 1991), ca. 2639 Ma (Ducharme et al. 1997), and ca. 2628 Ma (Davis 2021) cross-cut S2 and provide the minimum age constraint for D2 in the southern Abitibi and the Val-d'Or area. The final deformation period is characterized



# Orogenic gold mineralization in the Val-d'Or vein field

The intermediate to mafic-felsic volcanic and intrusive rocks of the VVF (Figs. 1b and 2) host ~46.8 Moz (1460 t) of gold in second to third order reverse shear zones associated with the LLCfz, which contain brittle-ductile, fault-fill shear, and associated extensional quartz-tourmaline-carbonate (QTC) veins (Robert 1989, 1990, 1994; Gosselin and Dubé 2005; Dubé et al. 2007; Monecke et al. 2017; Dubé and Mercier-Langevin 2020). Wallrocks commonly display igneous assemblages composed of varying proportions of plagioclase-quartz-alkalifeldspar-biotite-hornblende-ilmenite-titanomagnetite-magnetite that underwent greenschistfacies metamorphism (Robert 1983; Robert and Brown 1984, 1986a, b; Dubé 2018). These fault-fill, brittle-ductile shear veins dip to the south, strike E-W, and are sub-parallel to oblique to the penetrative S2 foliation that formed towards the peak of the N-S shortening event, syn- to late-D2, at  $2643 \pm 3$  Ma based on compiled xenotime dates (Fig. 2; Herzog et al. 2023). The veins display m-wide, strongly chloritized to quartz-tourmaline-albite-muscovite-pyrite alteration halos. Sulfide mineral assemblages commonly consist of pyrite ± pyrrhotite ± chalcopyrite-sphalerite ± galena and minor late-stage chalcopyrite-sphalerite ± galena. Gold is hosted dominantly as native Au ± Ag or Au-Te inclusions in pyrite and as native gold in quartz or tourmaline (Fig. 3, 4, 5; Robert 1983; Robert and Brown 1984, 1986a, b; Robert et al. 2005; Rezeau et al. 2017; Dubé 2018; Daver et al. 2020). A texturally late polymetallic gold-chalcopyritecarbonate ± sphalerite ± galena assemblage is commonly developed in sulfide fractures, which formed at  $2607 \pm 5$  Ma and post-dates the major syn- to late-D2 hydrothermal gold mineralization period (Herzog et al. 2023).

# Sampling and analytical techniques

# Mine sites, field samples, and petrography

For this study, representative sulfide mineral assemblages from the orogenic gold ores were examined for their relationships with gold-hosting veins and the vein-hosting structural fabric. Five orebodies hosting QTC veins (Goldex, Triangle, Plug #4, Beaufor, Pascalis Gold Trend) were sampled from drill cores. The vein sets, summarized in Table 1, are described in more detail in Herzog et al. (2023). Further



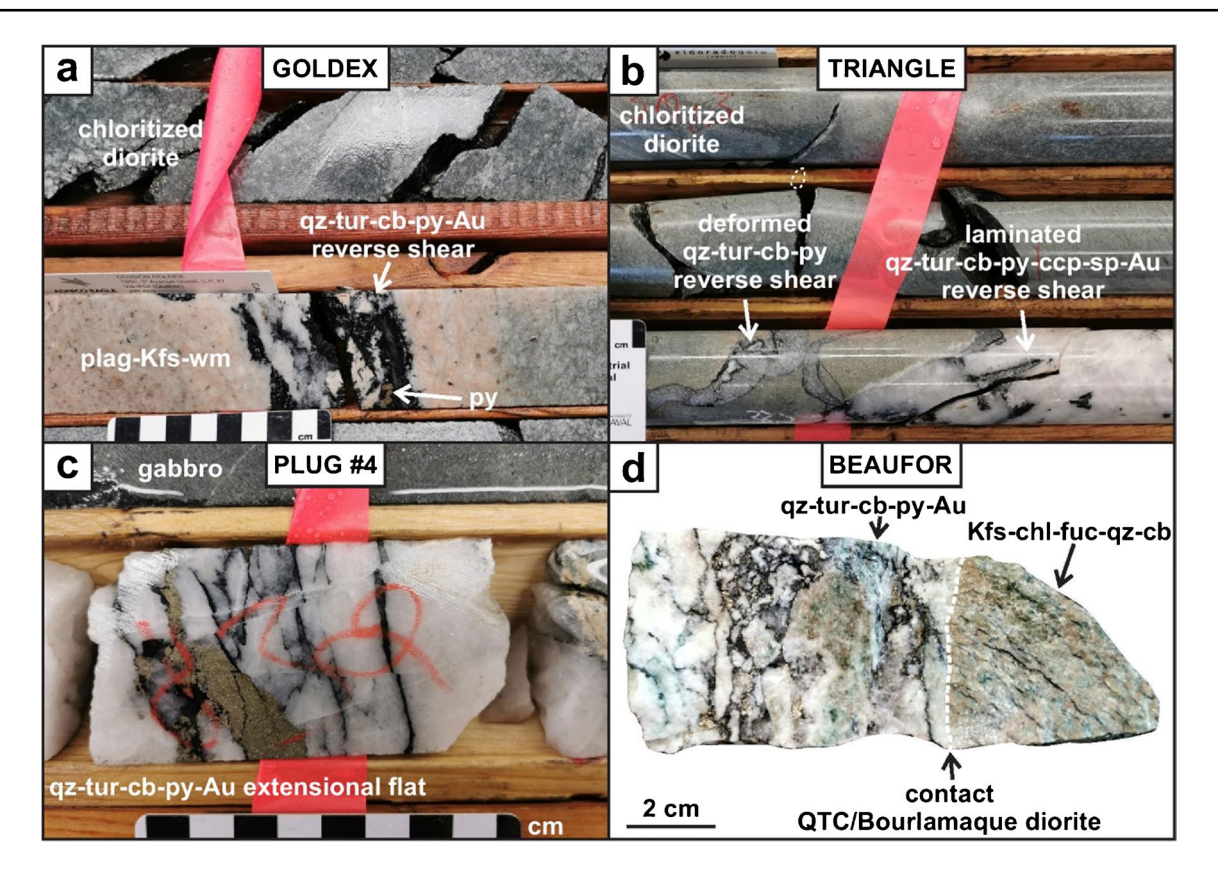


**Fig. 3** Field, core, and sample photographs showing key relationships between host rocks and hydrothermal quartz-tourmaline-carbonate veins at **a** Goldex, **b** Triangle, **c** Plug #4, and **d** Beaufor. Cb=carbonate, ccp=chalcopyrite, chl=chlorite, fuc=Cr-bearing phyllo-

silicate, gn=galena, Kfs=K-feldspar, plag=plagioclase, py=pyrite, qz=quartz, sp=sphalerite, tur=tourmaline. QTC=quartz-tourmaline-carbonate vein

material is presented in Electronic Supplementary Materials 1 and 2 (ESM1, Fig. 1; ESM2, Tables 1 and 2). Major sulfide parageneses were established. Detailed characterization of 26 samples by reflected light using a Zeiss Axio Imager M2 was completed to determine the sulfide mineralogy, texture, and paragenesis. Five epoxy mounts were prepared that contained 26 cylindrical rock cores, 6 mm in diameter, which were extracted from characterized samples. The five epoxy mounts were characterized for their major element composition, internal heterogeneity, texture and zonation using energy-dispersive-spectroscopy (EDS), and backscattered electron imaging (BSE) under analytical conditions of 20 kV and 175.9 μA in a FEI F50 scanning electron microscopy (SEM) at the Laboratoire de Microanalyse (Université Laval).

#### Sulfide mineral chemistry

The sulfide samples were analyzed at Laboratoire de Microanalyse, for their major and minor element compositions using a CAMECA SX-100 electron probe micro-analyser (EPMA) that is equipped with five wavelength-dispersive spectrometers. The beam size was 10 µm and beam conditions at 15 kV and 20 nA. Elements of interest for spot analyses included S, Mn, Fe, Co, Ni, Cu, Zn, Pb, As, and Sb (ESM2, Table 6). A total of 64 spot and line analyses of uncoated sulfide minerals followed using a RESOlution 193 nm ArF Excimer laser system (Applied Spectra) equipped with a S-155 large volume ablation cell (Laurin Technic), and coupled to an Agilent 7900 ICPMS, at the LabMaTer (Université du Québec à Chicoutimi). Thirty-four analytes were collected at beam sizes varying between 19 and 55 µm with a pulse rate of 15 Hz, a scan speed of 10 to 15 µm/s and a fluence of 3 J/cm<sup>2</sup>. To calculate quantitative sulfide trace element concentrations for line and spot analyses, three reference materials were used as calibrants: Laflamme PO-727 (a synthetic sulfide doped with  $\sim 40 \,\mu\text{g/g}$ PGEs, Memorial University), MASS1 (Wilson et al. 2002), and the USGS basaltic glass GSE-1 g (Guillong et al. 2005) using preferred values from the GEOREM database (Jochum et al. 2005) and Fe was used as internal standard based on EPMA analyses. LA-Q-ICPMS data was reduced through Iolite v4 and averaged values (ppm) for each sulfide domain are reported (Table 2; ESM2, Table 3; Woodhead et al. 2007; Paton et al. 2011). Three synthetic sulfides, UQAC-FeS1, UQAC-FeS5 (Savard et al. 2018), and MSS5 (Mungall



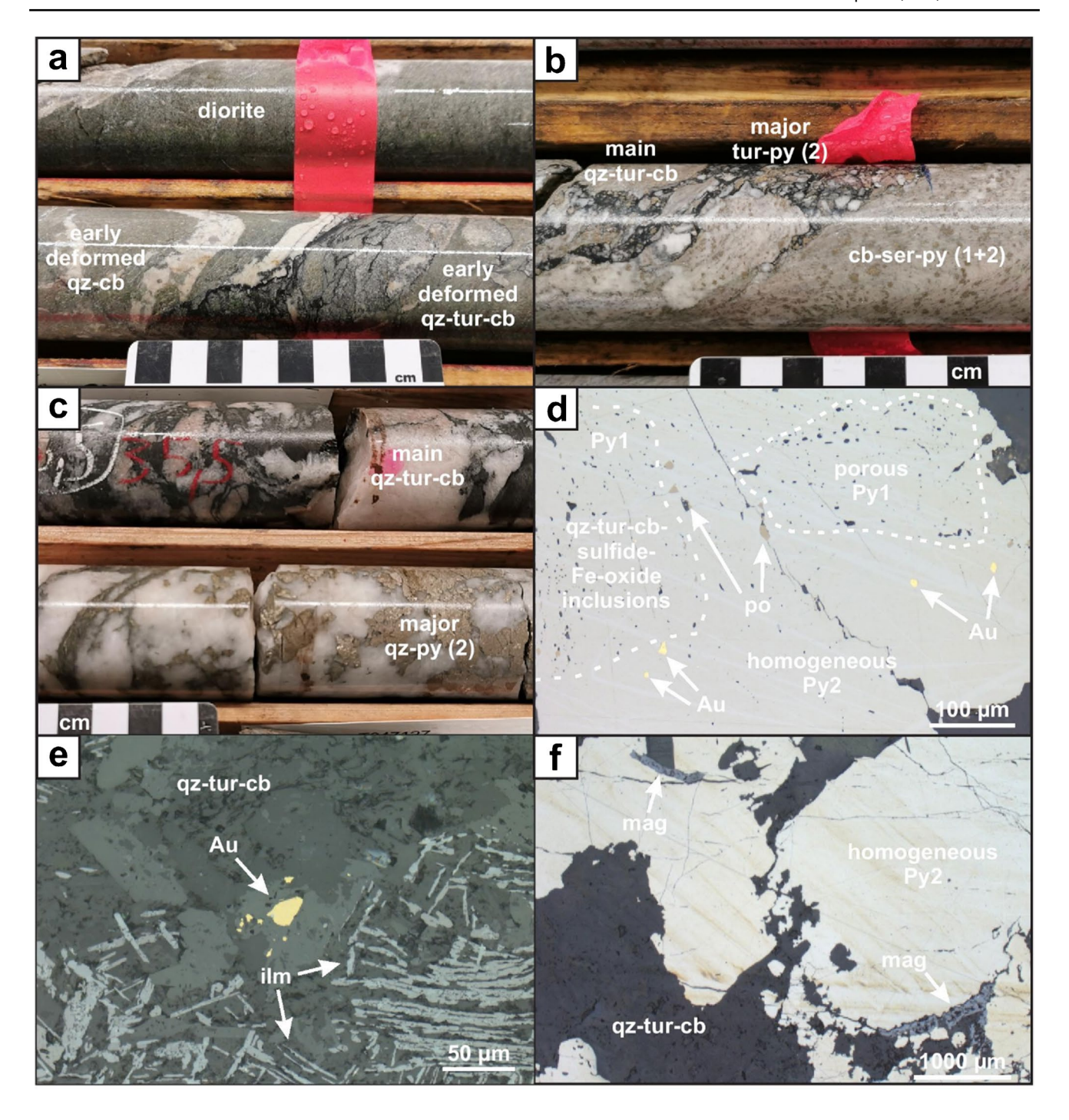


**Fig. 4** Common paragenesis of quartz-tourmaline-carbonate veins at the Goldex, Triangle, Plug #4, Pascalis Gold Trend, and Beaufor orebodies, particularly well developed in intrusive host rocks. **a** Early, highly deformed quartz-carbonate veins are commonly cross-cut by a set of deformed, unmineralized quartz-tourmaline-carbonate veins (Triangle). **b** Major gold mineralization hosted in strongly altered wallrock, consisting of primarily carbonate and white mica that host pyrite with a barren, porous Py1 core and Au-bearing, homogeneous Py2 rim (Triangle). **c** Bulk of the gold within brittle-ductile, laminated shear veins is commonly associated with the tourmaline- and

quartz-rich parts of the veins, hosting sulfide aggregates of several cm to dm, primarily composed of pyrite-rich assemblages (Triangle).  $\mathbf{d}$  Porous Py1 core in pyrite, hosting quartz-tourmaline-carbonate as well as sulfide and Fe-oxide inclusions, with a homogeneous Py2 rim overgrowth that contains bulk of the native Au and polymetallic inclusions (Triangle).  $\mathbf{e}$  Native Au associated with ilmenite in quartz-tourmaline-carbonate vein (Plug #4).  $\mathbf{f}$  Homogeneous Py2 rim overgrowth of magnetite (Plug #4). Au=gold, cb=carbonate, ilm=ilmenite, mag=magnetite, qz=quartz, ser=white mica, tur=tourmaline



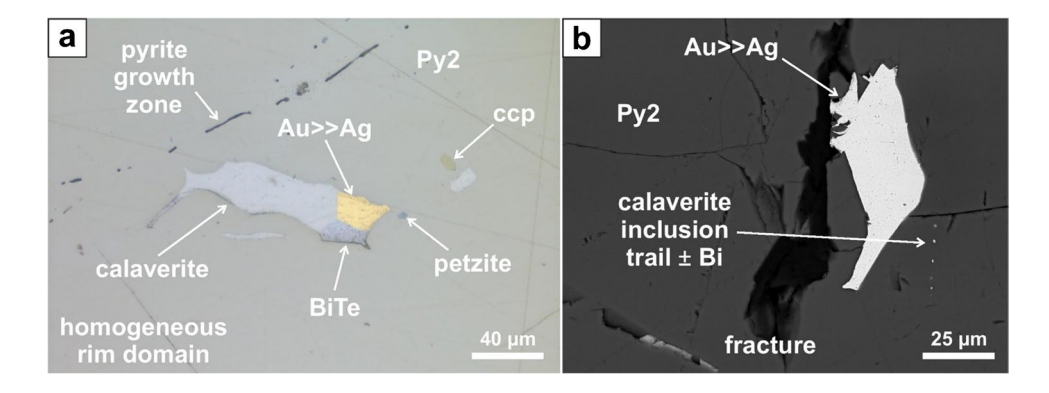


Fig. 5 Polymetallic inclusions (Au–Ag-Te-Bi) with gold in homogeneous Py2 rims, contain calaverite, minor petztite, and various BiTe polytypes with minor base metal sulfides such as chalcopyrite. **a** Reflected light photomicrograph of a typical calaverite-Au $\pm$ Ag $\pm$ Bi

inclusion in Py2 contained in the Plug #4 orebody. **b** Back-scattered electron image of Py2 from the Goldex orebody containing a trail of small calaverite inclusions and native gold grain

and Brenan 2014), along with GSE-1 g, were also used to assess quality control of the individual laser sessions and are compiled in ESM1, Figs. 6 and 7. In addition to the line and spots, analysis high-resolution quantitative maps of five samples were conducted on selected sulfides grains (ESM1, Figs. 2, 3, 4, and 5). The newly developed method (LA-FF-ICP-TOF-MS) is described in detail in Savard et al. (2023) and Paul et al. (2023) and summarized in ESM1.

### Multiple sulfur isotope analyses

In situ multiple sulfur isotope ratios for 91 spots in pyrite (Table 2; ESM2, Table 3) were acquired on a CAMECA IMS1280 Secondary Ion Mass Spectrometer (SIMS), at the Centre for Microscopy, Characterisation and Analysis at the University of Western Australia. The epoxy mount was trimmed at 1 cm and combined with a standard block containing matrix-matched sulfide mineral reference materials including (LaFlamme et al. 2016): Sierra pyrite ( $\delta^{33}$ S = 1.09 ± 0.15‰;  $\delta^{34}$ S = 2.17 ± 0.28%;  $\delta^{36}$ S = 3.96 ± 0.60%) and Nifty-b chalcopyrite ( $\delta^{33}$ S =  $-1.78 \pm 0.21\%$ ;  $\delta^{34}$ S =  $-3.58 \pm 0.44\%$ ;  $\delta^{36}$ S =  $-7.15 \pm 0.63\%$ ). The mount was trimmed to a thickness of 4 mm and coated with 30 nm of Au. The sample surface was sputtered over a 5×5 µm area with a 10 kV, Gaussian Cs<sup>+</sup> beam with intensity of ~2.5 nA, and total impact energy of 20 kV. Secondary ions were admitted in the double focusing mass spectrometer within a 75 µm entrance slit and focused in the center of a 3000 µm field aperture (×130 magnification). Energy was filtered using a 40 eV band pass with a 5 eV gap toward the high-energy side. All sulfur isotopes were collected simultaneously: <sup>32</sup>S, <sup>33</sup>S, and <sup>34</sup>S in Faraday cup detectors fitted with  $10^{10} \Omega$  (L2,  $^{32}S$ ) and  $10^{11} \Omega$  (L1,  $^{33}S$ , and H1,  $^{34}S$ ) resistors, and <sup>36</sup>S in an electron multiplier (H2), all operating at a mass resolution of  $\sim 2500$ . The  $^{32}S^{1}H$  and  $^{33}S$  peaks are not completely resolved under these conditions; thus, the magnetic field was offset slightly to the low-mass side to avoid interference from <sup>32</sup>S<sup>1</sup>H on the <sup>33</sup>S peak. The magnetic field was regulated using NMR control. Each analysis includes a pre-sputtering over a 10×10 µm area during 30 s, followed by the automatic centering of the secondary ions in the field aperture. Each analysis then consists of a 30 four-second cycles acquisition. Unknown sample material measurements were interspersed with matrix-matched reference material (Sierra pyrite and Nifty-b chalcopyrite). The Sierra pyrite and Nifty-b chalcopyrite were then used to monitor standard repeatability and analytical drift and to correct for instrumental mass fractionation (ESM1). Calculations for the  $\delta^{34}$ S,  $\Delta^{33}$ S, and  $\Delta^{36}$ S values are compiled in ESM2. Table 4. The average measurement errors (2 $\sigma$ ) of the unknowns yield uncertainties for  $\delta^{34}$ S  $(\pm 0.30\%)$ ,  $\Delta^{33}$ S  $(\pm 0.20\%)$ , and  $\Delta^{36}$ S  $(\pm 0.41\%)$ . The calculations for the absolute, in situ, propagated errors for  $\delta^{34}$ S.  $\Delta^{33}$ S, and  $\Delta^{36}$ S are outlined in LaFlamme et al. (2016).

High-precision bulk pyrite multiple sulfur isotope analyses ( $^{32}$ S,  $^{33}$ S,  $^{34}$ S, and  $^{36}$ S; n = 10) were acquired from QTC veins (ESM2, Table 5) described in Beaudoin and Pitre (2005). The pyrite samples were analyzed at McGill University and analyses followed the multiple sulfur analytical protocol outlined in Helt et al. (2014) and are summarized in ESM1. The analytical uncertainty (1 $\sigma$ ) for both,  $\delta^{34}$ S and  $\Delta^{33}$ S values, was  $\pm 0.02\%$ .

The  $\Delta^{36}S$  data for in situ and bulk multiple sulfur isotope analyses are reported in ESM2 but not further discussed due to their large absolute errors.

### **Results**

# Sulfide paragenesis and relationships of auriferous quartz-tourmaline-carbonate veins

A hydrothermal paragenesis of sulfide and wallrock alteration assemblages was established for each orebody and is



Table 1 Major sulfide mineral parageneses and associated sulfide mineral textures recorded in each orebody

Mineralization style	Orebody	Relative sulfide paragenesis	Sulfide texture	Mineral assemblage
Quartz-tourmaline-carbonate vein	Goldex	Py1a	Anhedral, homogeneous to minor heterogeneous zones, strongly frac- tured, irregular rim, no inclusions	qz-tur-cb-py-ccp
		Py1b	Euhedral, eroded rim, homogeneous, porous core, and homogeneous rim, tur-cb inclusions	qz-tur-cb-py-Au
		Py2	Euhedral, weakly irregular rim, weakly fractured, rt inclusions, sub- parallel to foliation	qz-cb-py-rt
	Triangle	Py1	Euhedral, homogeneous silicate inclu- sions, weakly eroded rim, weakly fractured, replaced by Py2 and forms porous core	qz-cb-py-ccp
		Py2	Sub-euhedral, homogeneous to minor heterogeneous zonation, strongly fractured, strongly eroded rim, porous core, cb-tur inclusions	qz-tur-cb-py-ccp-po-sch-rt-Au
		Ccp3	Anhedral, homogeneous, hosted in Py1 and Py2 fractures	qz-cb-ccp
	Plug #4	Py1	Euhedral, homogeneous silicate inclu- sions, weakly eroded rim, weakly fractured, replaced by Py2 and forms porous core	qz-cb-py-ccp-sch-mt-po
		Py2	Sub-euhedral, homogeneous to minor heterogeneous zonation, strongly fractured, strongly eroded rim, porous core, cb-tur inclusions	qz-tur-cb-py-ccp-po-sch-rt-tellurides Au
		Ccp3	Anhedral, homogeneous, hosted in Py1 and Py2 fractures	qz-cb-ccp
	Pascalis Gold Trend	Py1	Euhedral, homogeneous, minor porous core, weakly eroded rim, weakly fractured, ccp inclusions, replaced by Py2	qz-tur-cb-py-po-ccp-mag
		Py2	An-sub-euhedral, homogeneous, porous core, weakly to strongly fractured, strongly eroded rim, cb- tur-ccp inclusions, replaced by Ccp3	qz-tur-cb-py-po-Au
		Ccp3	Subhedral, homogeneous, strongly eroded rim, weakly fractured, hosted in Py1 & Py2 fractures and rims	cb-qz-py-ccp-rt
	Beaufor	Py1	Anhedral, homogeneous, silicate-cb inclusions, strongly eroded rim, strongly fractured	qz-chl-py-ccp-mol
		Py2	An-subhedral, homogeneous to minor heterogeneous zonation, strongly fractured, strongly eroded rim, cb- tur-ccp inclusions	qz-tur-cal-ank-dol-py-po-ccp-sch-Autellurides
		Ccp3	Minor, anhedral, homogeneous, hosted in Py1 and Py2 fractures	qz-cb-ccp

Ab = albite, Ag = silver, ank = ankerite, Au = gold, bt = biotite, bn = bornite, cal = calcite, cb = carbonate, ccp = chalcopyrite, chl = chlorite, dol = dolomite, ep = epidote, gn = galena, hem = hematite, mag = magnetite, mol = molybdenite, po = pyrrhotite, py = pyrite, qz = quartz, rt = rutile, sch = scheelite, sp = sphalerite, tur = tourmaline

summarized in Figs. 3 and 4. More detailed descriptions of sulfide mineral textures are in Table 1 as well as in ESM2, Tables 1 and 2.

The Goldex, Triangle, Plug #4, Pascalis Gold Trend, and Beaufor orebodies host gold in association with QTC veins (Fig. 4a), which contain pyrite-rich sulfide assemblages (>95 vol%) within cm- to dm-sized pyrite aggregates. These pyrite aggregates can form within the laminated vein or occur within altered wallrock, particularly in "seriticized" or tourmalinized areas (Figs. 3a–d and 4b–c). Vein alteration halo assemblages include pervasive quartz- "sericite"-albitechlorite-carbonate and minor Cr-bearing phyllosilicates



**Table 2** Summary of in situ multiple sulfur isotopic and trace element compositions (detection limit < 100 ppb) recorded in pyrite (Py1, Py1a, Py1b, Py2), and bulk pyrite multiple sulfur isotopic compositions

and a second	control d																	
Orebody	Relative sulfide paragen- esis	$\delta^{34}S$ (%0) $2\sigma$ $\delta^{34}S$ (%0) $2\sigma$ MIN MAX	2σ	δ <sup>34</sup> S(%ο) MAX	2σ	Δ <sup>33</sup> S (%o)	2σ 1	Δ <sup>33</sup> S (%0) 2σ MAX		Co (ppm)	Ni (ppm)	As (ppm)	Se (ppm)	Co (ppm) Ni (ppm) As (ppm) Se (ppm) Sb (ppm) Te (ppm) Bi (ppm) Au (ppm) Ag (ppm)	Te (ppm)	Bi (ppm)	Au (ppm)	Ag (ppm)
Goldex	Py1a+b	-0.4	0.3	0.4	0.3	-0.13	0.07	-0.02	0.05 4	424	635	33	9	p.u	8	8	30	2
	Py2	0.0	0.3	2.4	0.3	-0.15	0.11 (	0.01	0.11 1	1450	1700	125	220	100	145	230	1250	5
	Bulk			0.2	0.04		•	-0.03	0.04									
Triangle	Py1	0.0	0.3	3.5	0.3	-0.03		0.23		2000			50			15	p.u	3
	Py2	2.5	0.3	4.3	0.3	-0.16		-0.01	٠,		300		75	35	75	50	115	25
Plug #4	Py1	2.2	0.3	3.4	0.3			-0.08	0.10	128			4			5	11	17
	Py2	3.1	0.3	4.6	0.3	-0.15		-0.03	0.11 4	401		148	268	1		1120	160	71
Pascalis	Py1	4.9	0.3	5.2	0.3			0.01	0.05 4	4500			p.u			50	p.u	10
Gold	Py2	3.5	0.3	5.2	0.3		0.05	-0.03	0.05 8	0008	550	550	550			3000	165	205
Trend	Bulk			4.2	0.04		•	-0.03	0.04									
Beaufor	Py1	5.6	0.3	5.8	0.3	-0.12	0.111	-0.04		389	493	29	47	p.u		9	p.u	p.u
	Py2	5.9	0.3	6.3	0.3	-0.13	0.11	0.00	0.11 5	503	437	199	48	p.u	12	21	p.u	p.u
	Bulk			5.0	0.04			-0.01	0.04									
Louvi-	Bulk			1.3	0.04		•	-0.03	0.04									
court Gold- fields																		
Buffadis- son	Bulk			4.9	0.04		•	-0.04	0.04									
Sleepy Lake	Bulk			1.5	0.04		•	-0.07	0.04									
Wrightbar	Bulk			5.9	0.04			-0.01	0.04									
Nubell	Bulk			2.1	0.04		•	-0.06	0.04									
Canmet	Bulk			5.3	0.04		_	0.00	0.04									
Siscoe	Bulk			4.5	0.04		•	-0.05	0.04									

n.d. = below detection limit, Py = pyrite



(Fig. 3d). Pyrite commonly shows a porous core (Py1) with abundant carbonate, tourmaline and minor sulfides, including chalcopyrite, sphalerite, galena, and pyrrhotite as well as Fe-Ti-oxides such as ilmenite, titanomagnetite, and magnetite (Fig. 4d-f) and a homogeneous pyrite rim (Py2). Inclusion size and distribution of Py1 from veins strongly contrasts with that in wallrocks. Vein-hosted pyrite (Fig. 4d) shows erratically distributed, larger inclusion sizes up to hundreds of µm in size, whereas wallrock-hosted pyrite contains evenly distributed, smaller sized inclusions. The homogeneous Py2 rim hosts native Au and polymetallic Au-Ag-Te-Bi inclusions, primarily calaverite, which range from nm to µm in size (Fig. 5a-b). Both pyrite cores (Py1) and rims (Py2) are cross-cut by micro-fractures, which typically contain a chalcopyrite-carbonate-Au-Ag-Te-Bi ± sphalerite ± galena assemblage. At Goldex, the early Py1 can be divided into Py1a, which displays an anhedral texture and is fractured and inclusion-free. Py1b is euhedral with an irregular rim that commonly contains silicate, tourmaline, and carbonate, as well as rare native gold, inclusions. Py1b forms the porous core for Py2.

### **Sulfide mineral compositions**

In situ elemental analyses of chalcopyrite and pyrite from vein and alteration mineral assemblages at the Goldex, Triangle, Plug #4, Pascalis Gold Trend and Beaufor orebodies reveal that out of 34 measured analytes, only the elements Au, Ag, Te, Bi, Co, Ni, As, Se, and Sb (Table 2; ESM2, Table 3) occur above detection limits (<100 ppb) as minor (<10,000 ppm) and trace concentrations (<1000 ppm) in Py1 cores and Py2 rims. Only Py1b (Au  $\leq$  30 ppm) and Py1 (Au  $\leq$  11 ppm) cores hosted in Goldex and Plug #4, respectively, contain trace concentrations of Au. In general, Py2 rims contain the bulk of the gold as native gold or polymetallic gold inclusions (Fig. 6), which include major calaverite and minor petzite, with other Au-Ag-Bi-Te assemblages of various compositions (Au  $\leq$  1250 ppm; Ag  $\leq$  205 ppm; Te  $\leq$  2250 ppm; Bi  $\leq$  3000 ppm).

Goldex pyrite yields lower concentrations of Co ( $\leq$ 424 ppm) and Ni ( $\leq$ 635 ppm) in porous Py1a and Py1b (Table 2) compared to oscillatory zoned Co, Ni, and As in Py2 (Co  $\leq$  1450 ppm; Ni  $\leq$  1700 ppm; As  $\leq$  125 ppm). Homogeneous Py2 also contains areas of relatively high Se and Sb (both  $\leq$  220 ppm) concentrations. Gold occurs at low concentrations in Py1b ( $\leq$ 30 ppm) and within nanometer-sized polymetallic gold inclusions contained in Py2 (Fig. 5b).

Triangle pyrite displays locally distributed areas of Co ( $\leq$  2000 ppm), Ni ( $\leq$  400 ppm), and Se ( $\leq$  50 ppm) in porous Py1 (Table 2) and low concentrations of Co ( $\leq$  529 ppm), as well as oscillatory zoned Ni ( $\leq$  300 ppm) and As ( $\leq$  541 ppm) associated with homogeneous Py2. Visible

polymetallic inclusions and sporadic distribution of Sb ( $\leq$ 35 ppm) characterizes Py2.

Pyrite from Plug #4 yields primarily low concentrations of Co ( $\leq$  128 ppm) and Ni ( $\leq$  22 ppm) in porous Py1 and Py2 (Co  $\leq$  401 ppm; Ni  $\leq$  26 ppm), the latter of which also shows enrichment in As ( $\leq$  148 ppm) and Se ( $\leq$  897 ppm). Low concentrations of Au ( $\leq$  11 ppm), Ag ( $\leq$  17 ppm), Te ( $\leq$  22 ppm), and Bi ( $\leq$  5 ppm) occur in Py1, but no inclusions were observed. Py2 contains gold in visible polymetallic inclusions (Fig. 5a).

Porous Py1 from the Pascalis Gold Trend (Table 2) yields localized areas of minor concentrations in Co ( $\leq$ 4500 ppm) and Ni ( $\leq$ 550 ppm). Homogeneous Py2 shows oscillatory zones in Co ( $\leq$ 3300 ppm), Ni ( $\leq$ 2200 ppm), and As ( $\leq$ 550 ppm). One analyzed Py2 rim has the highest recorded concentration of Co (Fig. 6; Co  $\leq$ 8000 ppm) in all orebodies. Elevated concentrations of Co, Ni, and As (Fig. 6) in oscillatory zoned Py2 appear unrelated to inclusions.

Porous Beaufor Py1 primarily contains low trace concentrations of Co ( $\leq$  389 ppm) and Ni ( $\leq$  493 ppm). Homogeneous Py2 contains low Co ( $\leq$  503 ppm) and Ni ( $\leq$  437 ppm), but higher local concentrations of As ( $\leq$  199 ppm), Se ( $\leq$  48 ppm), and negligible Sb.

### Multiple sulfur isotope composition

In situ multiple sulfur isotopic composition of pyrite (n=91)from QTC veins at Goldex, Triangle, Plug #4, Pascalis Gold Trend, and Beaufor orebodies (Fig. 7a; ESM2, Table 3) shows a moderate range in  $\delta^{34}$ S (from – 0.4% to 6.3%; Fig. 7b) and a narrow range in  $\Delta^{33}$ S values (from – 0.20%) to 0.23%; Fig. 7c). Pyrite commonly yields a shift in  $\delta^{34}$ S values (< 3.0%), from Py1 cores to Py2 rims (Figs. 7a and 8; Table 2). Similarly, bulk pyrite multiple sulfur isotope analyses (Fig. 7a; Table 2) yield  $\delta^{34}$ S values from 0.6% to 6.0% and  $\Delta^{33}$ S from -0.07% to 0%. Both, in situ and bulk pyrite multiple sulfur isotope data, have a similar range in sulfur isotopic compositions, with a systematically small, mostly negative deviation in  $\Delta^{33}$ S, outside the field for mass-dependent fractionation of sulfur (MDF-S). The analytical uncertainty (2 $\sigma$ ) for negative  $\Delta^{33}$ S values overlaps with the MDF-S field, such that care must be exercised in interpretation.

Sulfur isotope analyses of pyrite (n=29) from the Goldex orebody show the lowest  $\delta^{34}$ S values  $(-0.4\%_o$  to  $0.5\%_o)$  that are associated with the barren Py1a and Py1b core domains (Fig. 8c). Higher  $\delta^{34}$ S values  $(0.0\%_o$  to  $2.4\%_o)$  characterize Py2 rims (Fig. 7a; Table 2). Both pyrite domains yield a consistent negative  $\Delta^{33}$ S range between  $-0.15\%_o$  and  $0.01\%_o$ .

Py1 core hosted in altered diorite wallrock of the Triangle orebody (Fig. 8a) records a  $\delta^{34}$ S value of -0.1% (Fig. 7a) and the highest  $\Delta^{33}$ S value (0.23%) of all QTC orebodies and in general range between 0.6% and 3.5%, with  $\Delta^{33}$ S



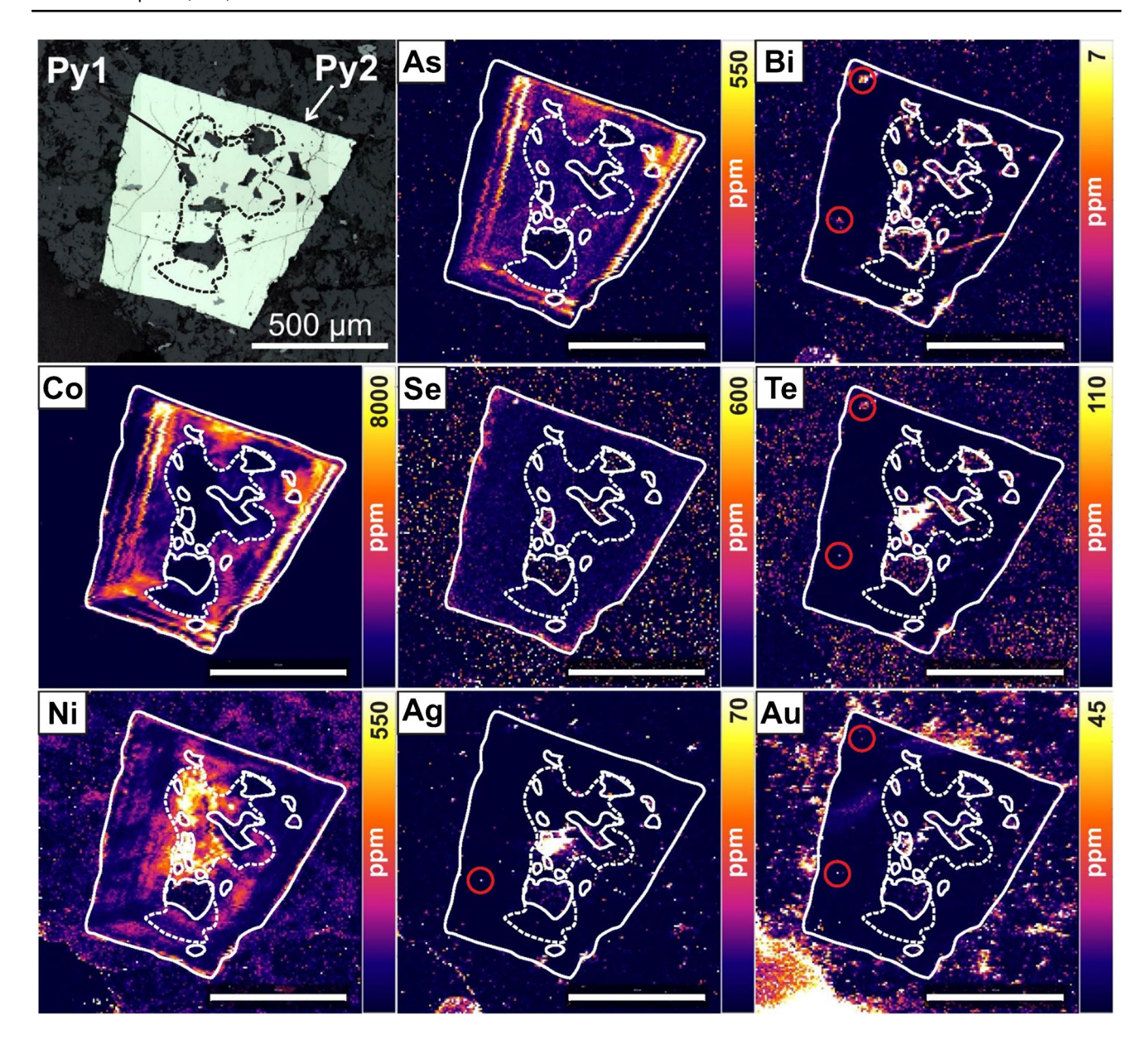


**Fig. 6** Reflected light photomicrograph, qualitative, and quantitative LA-FF-ICP-TOF-MS maps of Py1 and Py2 from Pascalis Gold Trend (PGT\_34), showing the key minor and trace elements As, Bi, Co, Se,

Te, Ni, Ag, and Au in the quartz-tourmaline-carbonate veins. Red circles indicate areas hosting polymetallic inclusions (Au-Ag-Te-Bi)

values between -0.03% and 0.11% (n=9). This single outlier could also be explained if a Py1 inclusion was measured during in-situ sulfur isotope analysis. The Py2 rim shows higher  $\delta^{34}$ S values (up to 4.3%) and negative  $\Delta^{33}$ S values (>-0.16%). Higher  $\delta^{34}$ S and negative  $\Delta^{33}$ S values commonly characterize vein-hosted Py2 (n=16; Fig. 7a; Table 2).

Vein pyrites from Plug #4 (n=14) show lower  $\delta^{34}$ S values recorded in Py1 cores (2.2‰) compared to higher values in Py2 rims (up to 4.6‰). Both pyrite domains display a small negative  $\Delta^{33}$ S range between -0.20% and -0.03% (Fig. 7a; Table 2).

Pyrite domains Py1 and Py2 from the Pascalis Gold Trend orebody (n=14) display a narrow range in  $\delta^{34}$ S values, between 5.2‰ and 3.5‰, respectively (Fig. 7b), and  $\Delta^{33}$ S values range between -0.16% and 0.01% (Fig. 7a; Table 2).

Vein pyrites at Beaufor (n=9) display lower  $\delta^{34}$ S values in Py1 core (> 5.6%) and higher  $\delta^{34}$ S values in the Py2 rim (<6.3%). Both pyrite domains show negative  $\Delta^{33}$ S values (> -0.13%; Fig. 7a; Table 2).

Bulk pyrite multiple sulfur data from vein pyrite samples (Table 2; ESM2, Table 5; n = 10) described in Beaudoin and Pitre (2005) yield a similar range in  $\delta^{34}$ S values



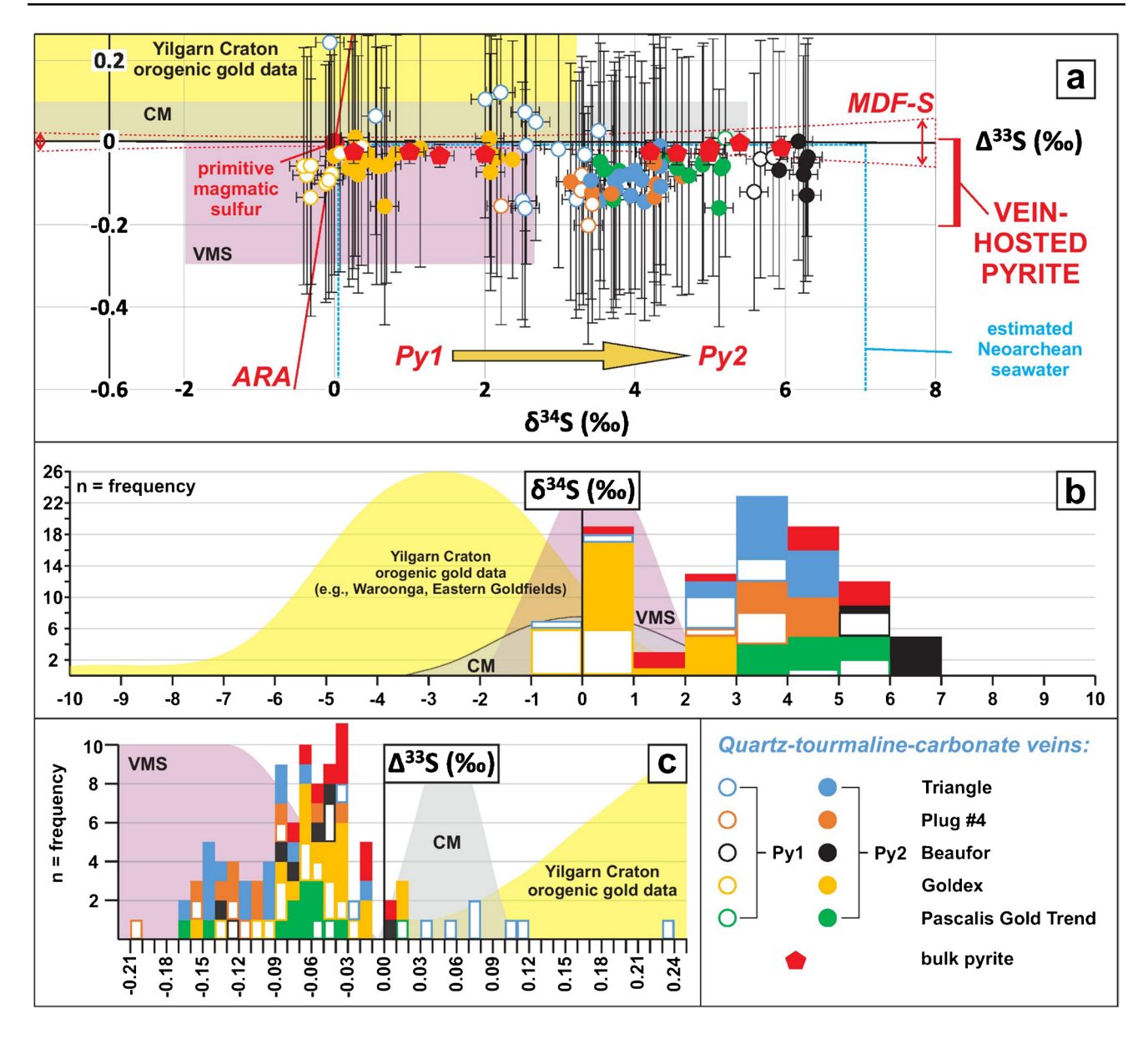


Fig. 7 a A  $\delta^{34}S$  vs.  $\Delta^{33}S$  plot showing multiple sulfur isotope data (pyrite) for Py1 and Py2 associated with quartz-tourmaline-carbonate veins (Triangle, Plug #4, Beaufor, Goldex, Pascalis Gold Trend) and alteration halos (Triangle) from the VVF. Outline of the mass-dependent fractionation field for sulfur (MDF-S, LaFlamme et al. 2018b). Error bars (2 $\sigma$ ) display the overall analytical uncertainties. All individual SIMS spot and bulk pyrite analyses are in Table 2 and ESM 2. Bulk multiple sulfur isotope data for Canadian Malartic (CM, Helt 2012; Helt et al. 2014), volcanogenic massive sulfide deposits (VMS, Sharman et al. 2015) of the Abitibi subprovince, as well as primitive magmatic sulfur with a composition of  $\delta^{34}S$ =0% and

 $\Delta^{33}S = 0\%$  (Labidi et al. 2013; Fiorentini et al. 2018) and the estimated range of Neoarchean seawater yielding values of  $\delta^{34}S > 0\%$  and  $\Delta^{33}S < -1.5\%$  (Jamieson et al. 2013). **a** A  $\delta^{34}S$  vs.  $\Delta^{33}S$  plot for both pyrite generations hosted within quartz-tourmaline-carbonate veins. The golden arrow indicates observed sulfur isotope evolution trends from porous Py1 cores towards homogeneous Py2 rims. ARA = Archean Reference Array of  $\Delta^{33}S \approx 0.89*\delta^{34}S$  (Ono et al. 2009). Bulk and in situ multiple sulfur isotope data from orogenic gold deposits hosted in the Yilgarn Craton compiled in LaFlamme et al. (2018c). **b** Frequency plot of  $\delta^{34}S$  values for each orebody. **c** Frequency plot of  $\Delta^{33}S$  values for each orebody

(between 0.2% and 5.9%) and a narrow range in  $\Delta^{33}$ S values (between – 0.07% and 0%). Pyrite from Goldex, Lucien-Béliveau (extension of the Pascalis Gold Trend),

and Beaufor have bulk  $\delta^{34}$ S (0.2%, 4.2%, and 5.0%, respectively) and  $\Delta^{33}$ S (-0.03%, -0.03%, and -0.01%,



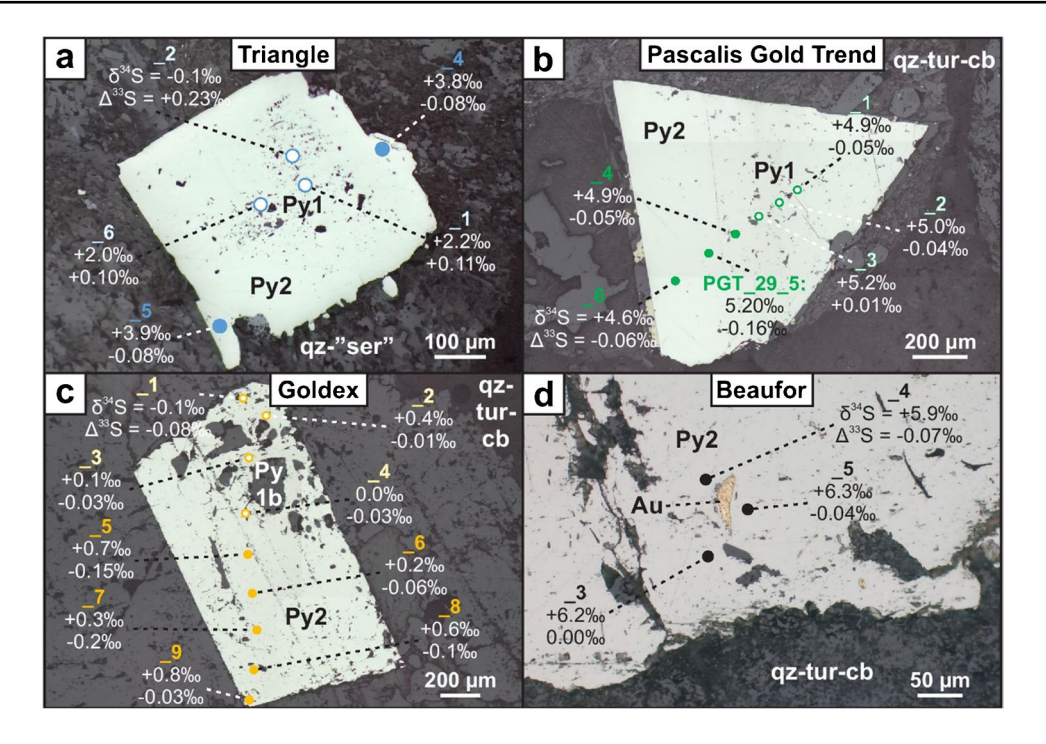


**Fig. 8** Reflected light photomicrographs showing key sulfide mineral assemblages and in-situ SIMS analyses. Empty symbols represent texturally early Py1 and filled symbols texturally late Py2 associated with native Au inclusions. **a** Pyrite hosted in altered quartz-sericite alteration halo at the Triangle orebody. Early, porous Py1 core with abundant silicate inclusions shows slightly lower  $\delta^{34}$ S and significantly higher  $\Delta^{33}$ S values compared to the homogeneous Py2 rim that hosts polymetallic inclusions ( $2\sigma$ :  $\delta^{34}$ S < 0.3% $_{e}$  and  $\Delta^{33}$ S < 0.10% $_{e}$ ; analysis number LQ\_20\_x). **b** Pyrite hosted in quartz-tourmalinecarbonate vein at Pascalis Gold Trend, showing porous Py1 core and

respectively) values within the range recorded in Py1 and Py2 by in situ multiple sulfur analyses (Fig. 7a–c).

#### **Discussion**

Most commonly proposed fluid mechanisms associated with sulfide and gold precipitation in orogenic gold systems include fluid mixing (e.g., Cameron and Hattori 1987; Beaudoin and Pitre 2005; Neumayr et al. 2008; Beaudoin and Chiaradia 2016), fluid boiling and immiscibility (Peterson and Mavrogenes 2014; Sugiono et al. 2022), and fluid-rock reactions (Phillips 1986; Ward et al. 2017). Orogenic gold systems in meta-sedimentary rock successions commonly incorporate Au as "invisible gold" through coupled Au-As redox reactions into As-rich sulfides (e.g., Pokrovski et al. 2019, 2021), whereas in meta-volcanic rocks, gold frequently occurs in the form of polymetallic (Au-Ag-Te-Bi) inclusions in As-poor sulfides, suggesting different fluid mechanisms to precipitate gold (e.g., Bi et al. 2011; Sherlock et al. 2012). These processes have an important bearing on fO2 and/or fS2 conditions of a hydrothermal fluid and homogeneous Py2 rim. Both domains have a narrow range in  $\delta^{34}S$  and negative  $\Delta^{33}S$  signature  $(2\sigma: \delta^{34}S < 0.3\%e$  and  $\Delta^{33}S < 0.05\%e$ ; analysis number PGT\_29\_x). **c** Early, porous pyrite core contains large tourmaline and carbonate inclusions, shows slightly lower  $\delta^{34}S$  values compared to the rim at Goldex. Both domains yield slightly negative  $\Delta^{33}S$  values  $(2\sigma: \delta^{34}S < 0.3\%e$  and  $\Delta^{33}S < 0.11\%e$ ; analysis number GX\_35\_x). **d** Homogeneous Py2 rim in a quartz-tourmaline-carbonate vein of the Beaufor orebody, which hosts a native Au inclusion and shows slightly higher  $\delta^{34}S$  and negative  $\Delta^{33}S$  values  $(2\sigma: \delta^{34}S < 0.3\%e$  and  $\Delta^{.33}S < 0.11\%e$ ; analysis number LB\_C481\_26R\_x)

accordingly gold solubility that control the style of orogenic gold deposits. Here, we examine the within-grain sulfide multiple sulfur isotope and trace element signatures to better understand hydrothermal fluid mechanisms that precipitate Au-Ag-Te-Bi-bearing sulfides in orogenic gold deposits.

# Gold-hosting pyrite and auriferous hydrothermal fluid signatures

The VVF includes several QTC vein orebodies including Goldex, Triangle, Plug #4, Pascalis Gold Trend, and Beaufor that are hosted in meta-volcanic and intrusive rocks (Fig. 3). These veins commonly display at least two texturally and chemically distinct sulfide generations (Table 2): a porous silicate, carbonate and minor sulfide, and Fe-oxide inclusion-bearing Py1 core, which is surrounded by a homogeneous Py2 rim (Fig. 4). The Py2 rim hosts most of the gold, either as native or polymetallic Au-Ag-Bi-Te inclusions (Fig. 5; e.g., Robert 1983; Robert and Brown 1984, 1986b; Rezeau et al. 2017; Daver et al. 2020). Robert and Brown (1986b) and Rezeau et al. (2017) recognized the precipitation of texturally late pyrrhotite at Sigma and Lac Herbin (Fig. 1b)



associated with the late stages of QTC vein formation, which coincides with the precipitation of Py2. This association of late homogeneous Py2 rims and pyrrhotite, and the lack of abundant hematite or acidic alteration halos (Figs. 3 and 4), imply that the pyrite-rich assemblages formed under reducing fluid  $fO_2$  and near-neutral pH conditions, within the pyrite stability field (Figs. 8, 9a).

The textural relationship between a porous pyrite core (Py1) surrounded by a homogeneous pyrite rim (Py2) is frequently documented in orogenic gold systems and interpreted to record coupled dissolution-reprecipitation reactions in sulfide minerals (e.g., McCuaig and Kerrich 1998; Goldfarb et al. 2001, 2005; Robert et al. 2005; Fougerouse et al. 2016). In many cases, pyrite dissolution and remobilization require interaction with a high fO2 and low pH (<5) hydrothermal fluid and an increase in fluid  $fS_2$  during the reaction, which will lead to reprecipitation of marcasite (Fougerouse et al. 2016; Wu et al. 2019). However, marcasite is not recorded in pyrite of the VVF. The erratically distributed, large-sized inclusions recorded in Py1 (Figs. 4d, 6 and 8b-d), the low variability in trace element compositions (Fig. 6), and consistent  $\Delta^{33}$ S signatures between Py1 and Py2 suggest that Py2, which overgrows Py1 and gangue minerals, was precipitated from an evolved hydrothermal fluid.

In the five investigated orebodies, Pv2 hosts most of the gold primarily in the form of polymetallic inclusions composed of calaverite and native gold with minor petzite. However, polymetallic inclusions that lack major Au-bearing tellurides can contain various proportions of Au ( $\leq 1250$  ppm), Ag ( $\leq 205 \text{ ppm}$ ), Te ( $\leq 2250 \text{ ppm}$ ), and Bi ( $\leq 3000 \text{ ppm}$ ). In Goldex (Py1b) and Plug #4 (Py1), low concentrations of lattice-bound Au could be identified ( $\leq 30$  ppm). Daver et al. (2020) noted pyrite rims and cores that contain similarly low concentrations for Ni ( $\leq 4000$  ppm), Co ( $\leq 700$  ppm), and As ( $\leq 100$  ppm) in pyrite from the Lac Herbin, Goldex, Beaufor, and Triangle orebodies (Fig. 1b). Moreover, it has been shown that As contents higher than 1000 ppm in pyrite facilitate the uptake of lattice-bound gold into pyrite through Au-As coupled redox reactions (Reich et al. 2005; Pokrovski et al. 2019, 2021; Wu et al. 2021). The low As contents recorded in Py1, Py1b ( $\leq$ 67 ppm), or Py2 ( $\leq$ 550 ppm) may, therefore, explain the formation of gold-bearing inclusions and nm- to µm-sized polymetallic inclusion trails within crystal lattice deficiencies developed during pyrite growth (Figs. 5 and 10a).

#### Multiple sulfur isotope signature of hydrothermal fluid

The  $\delta^{34}$ S values for Py1 cores and Py2 rims (Table 2) from the five orebodies are as follows: Goldex = -0.4% to 2.4%; Triangle = 0.0% to 4.3%; Plug #4 = 2.2% to 4.6%; Pascalis Gold Trend = 4.9% to 5.2%; and Beaufor = 5.6% to 6.3%. Mean  $\Delta^{33}$ S values (Table 3) are  $-0.03 \pm 0.17\%$ 

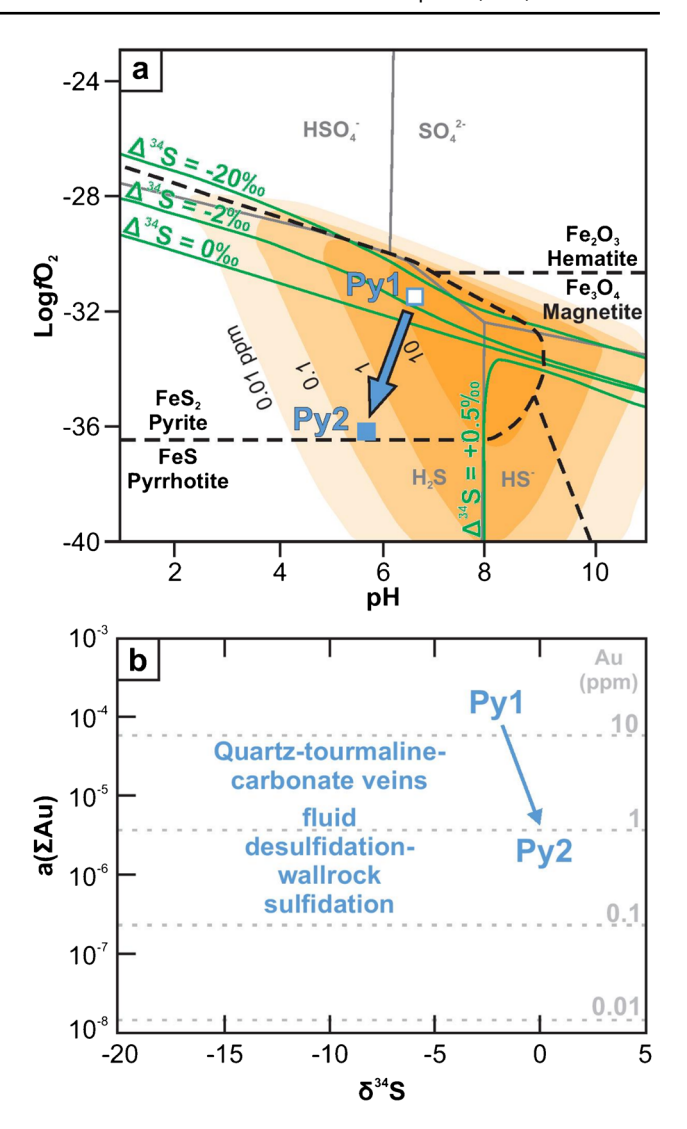


Fig. 9 a A fO<sub>2</sub>-pH diagram showing characteristic fluid conditions for orogenic gold mineralization. The blue arrow represents the hydrothermal fluid paths leading to gold deposition in quartztourmaline-carbonate veins of the VVF. Modified after Ohmoto (1972) and Hodkiewicz et al. (2009). The mineral stability fields of the Fe-O-S system and sulfur species are based on  $\Sigma S = 0.05$  mol/ kg, and solid green lines ( $\Delta^{34}$ S) represent contour lines of isotopic shifts in  $\delta^{34}$ Svalues. Gold solubility contour lines (in ppm) are taken from Shenberger and Barnes (1989). Further experimental conditions include T=300 °C, P=1 kbar,  $Na^+=1$  m,  $K^+=0.1$  m,  $Ca^{2+} = 0.01$  m, and  $\Sigma \delta^{34}S = 0\%$ . **b** Activity diagram showing the relationships between changes in δ.34S, related to the removal of H<sub>2</sub>S from a hydrothermal fluid, and total gold solubility  $(a(\Sigma Au))$  and the observed hydrothermal processes associated with gold precipitation in the quartz-tourmaline-carbonate veins. Modified after Palin and Xu (2000)

(2SD) for Py1 and  $-0.08 \pm 0.09\%$  (2SD) for Py2. This negative  $\Delta^{33}$ S signature (ranging from -0.20% to 0.01%) in pyrite-rich veins of the VVF (Fig. 7a–c) must be treated with caution due to single spot uncertainties within error of 0% and overlap with the MDF-S field (Fig. 7a). Even



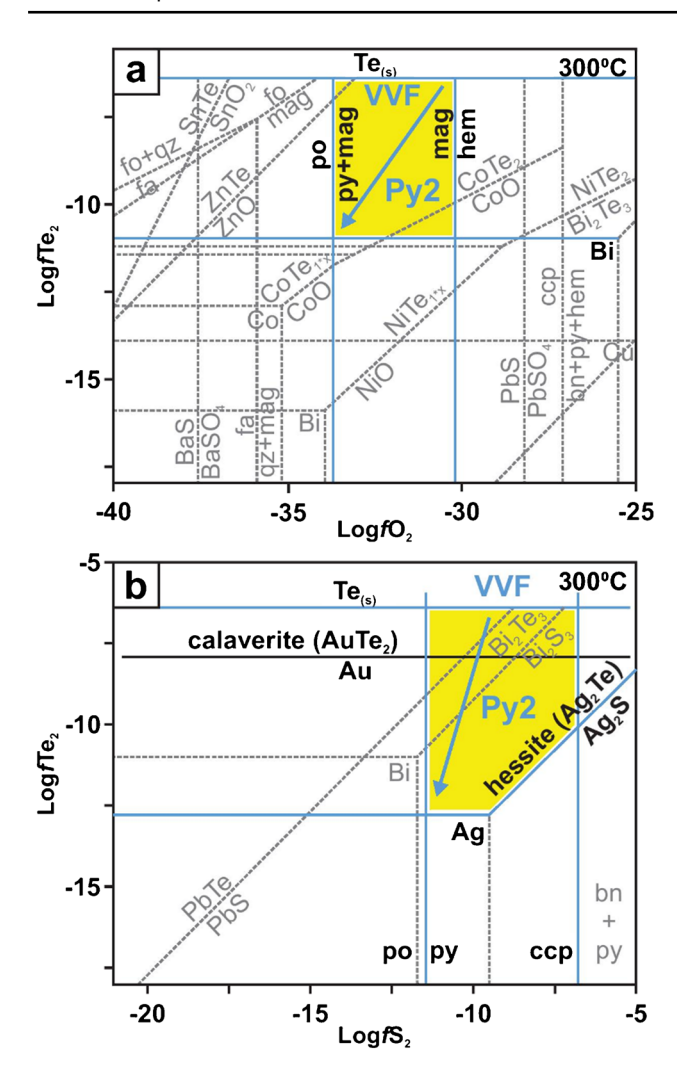


Fig. 10 a Diagram showing Au and As contents of Py1 and Py2 in log Au (mol%) vs. log As (mol%) space to determine gold solubility as a function of As-contents in pyrite. Modified from Reich et al. (2005) and Pokrovski et al. (2019). b A  $\log Te_2 - \log fS_2$  diagram showing the formation of increasingly Ag-rich tellurides during  $fS_2$  decrease and Py2 growth, at conditions of T=300 °C, P=1 bar. Modified from Afifi et al. (1988a). Bn=bornite; ccp=chalcopyrite; po=pyrrhotite; py=pyrite; VVF=Val-d'Or Vein Field

if systematic, the negative  $\Delta^{33}S$  signature could represent an apparent trend, which can result from SIMS drift correction, known to cause a variation of  $\pm\,0.1\%$  (Whitehouse 2013). Nonetheless, a similarly small and negative trend in bulk pyrite multiple sulfur data (Fig. 7a–c; Table 2; ESM2, Table 5) is consistent with the in-situ SIMS  $\Delta^{33}S$  values in the VVF.

The small negative range in  $\Delta^{33}$ S values is in contrast with bulk pyrite multiple sulfur isotope data by Helt (2012), reporting primarily positive  $\Delta^{33}$ S values, ranging from -0.01% to 0.11%, at the Pontiac sedimentary rockhosted Canadian Malartic deposit (Fig. 7a). Similarly, orogenic gold districts in the Yilgarn Craton commonly yield

Table 3 Overview of recorded mean, in situ, multiple sulfur isotopic, and sulfide trace element compositions recorded in relative sulfide paragenesis

Au	+	+
Bi	+	++
Te	+	++
As Se Te	+	+
As	+	+
ij	++	+
Co	+	+
2SD	0.53	0.55
$\Delta^{36}$ S (% $_o$ ) MEAN	-0.08	-0.17
2SD	0.17	0.09
$\Delta^{33}$ S (%o) MEAN	-0.03	- 0.08
2SD	4.2	3.6
δ <sup>34</sup> S (%ο) MEAN	2.1	3.3
Relative sulfide paragenesis	Py1, Py1a + b ( $\pm$ Au)	Py2 (Au)
Sulfide	pyrite	pyrite

A + +

+ + +, major concentration (>1 wt% or>10,000 ppm); + +, minor (<1 wt% or<10,000 ppm); +, trace (<0.1 wt% or<10000 ppm)



a consistent, positive  $\Delta^{33}S$  signature (Fig. 7), indicating a sulfur reservoir at least partially sourced from sedimentary rocks (Selvaraja et al. 2017; LaFlamme et al. 2018a, b; Sugiono et al. 2021; Caruso et al. 2022). The VVF is hosted by volcanic and intrusive rocks in which volcanogenic hydrothermal processes formed VMS deposits with negative  $\Delta^{33}S$  signature (Jamieson et al. 2006; Sharman et al. 2015). The  $\Delta^{33}S$  signature across the VVF indicates that the sulfur reservoir was homogeneous, consistent with a low variance source at depth (c.f., Pettke et al. 1999; Phillips and Powell 2010; Tomkins 2013; Pitcairn et al. 2015, 2021; Patten et al. 2020).

The restricted range of mean  $\delta^{34}S$  values of  $2.1 \pm 4.2\%$  (2SD) and  $3.3 \pm 3.6\%$  (2SD) recorded in Py1 cores and Py2 rims (Table 3), respectively, in the five orebodies (Fig. 7a) suggests the contribution of a homogeneous, reduced sulfur source. Sulfur derived specifically from sedimentary rocks commonly shows extremely variable  $\delta^{34}S$  signatures that reflect strong local controls, based on variations of  $\delta^{34}S$  values recorded in marine pyrite (e.g., LaFlamme et al. 2018a; Pasquier et al. 2021). Therefore, it is unlikely that the source of sulfur for the VVF is sourced entirely from sedimentary rocks. Rather, a common homogeneous sulfur source is suggested, which is in agreement with the small negative  $\Delta^{33}S$  signature recorded in the VVF.

# Fluid fO<sub>2</sub> and fS<sub>2</sub> control on gold precipitation in greenstone belts

Hydrothermal fluids associated with orogenic gold systems are typically reduced, lie within several magnitudes of the fayalite-magnetite-quartz buffer (FMQ to FMQ-4), and display an excess of reduced sulfur, particularly, HS $^-$ , H $_2$ S, and S $_3^-$  complexes, that transport gold (350  $\pm$  50 °C; Mikucki and Ridley 1993; Loucks and Mavrogenes 1999; Williams-Jones and Heinrich 2005; Evans et al. 2006; Pokrovski et al. 2014, 2015, 2022). A variety of physico-chemical fluid processes may lead to gold decomplexation from reduced auriferous fluids.

In the case of the VVF, there is no evidence for gold precipitation associated with fluid cooling or major pH fluctuations. Narrow, cm-, to m-wide QTC vein alteration halos lack acidic alteration assemblages (Figs. 3 and 4), suggesting a near-neutral pH as is common in orogenic gold systems (Goldfarb et al. 2001, 2005; Goldfarb and Groves 2015). Instead, as reduced auriferous fluids are seismically pumped through the crust (Sibson 1981; Sibson et al. 1988; Sibson and Scott 1998; Cox 2016), gold solubility is driven by either an increase in  $fO_2$  or a decrease in  $fS_2$ . An increase in  $fO_2$  of a hydrothermal fluid results in decomplexation of sulfur–gold complexes inducing deposition of Au (Palin and Xu 2000; Williams-Jones and Heinrich 2005; Sugiono et al. 2022). Similarly, a decrease in  $fS_2$  through the removal of

reduced sulfur from a hydrothermal fluid leads to a decrease in gold-sulfide complex activity (Seward 1989; McKibben and Eldridge 1990), which can significantly decrease gold solubility and lead to gold precipitation. Monitoring of changing fluid conditions using the pyrite  $\delta^{34}S$  and  $\Delta^{33}S$  values, in combination with Ni, Co, and As distributions and contents, can provide insights into the mechanisms that lead to gold deposition.

#### Fluid mixing

Studies have shown that fluid mixing between a reduced deep-seated fluid and a more oxidized magmatic fluid, or hypothesized meteoric fluid and seawater, can lead to destabilization of dissolved gold-sulfide complexes and lead to gold precipitation (Uemoto et al. 2002; Bateman and Hagemann 2004). It is possible to investigate fluid mixing using the  $\Delta^{33}$ S signature, whereby several products between different end-member sulfur reservoirs will produce variable  $\delta^{34}$ S- $\Delta^{33}$ S signatures (Cameron and Hattori 1987; Neumayr et al. 2008; LaFlamme et al. 2018c), and specifically a depleted  $\Delta^{33}$ S signature compared to the two end-members (Barré et al. 2021). Sulfur reservoirs that have been invoked as endmember sulfur sources associated with Neoarchean orogenic gold systems include seawater sulfate ( $\delta^{34}$ S between ca. 0%oand 7% and  $\Delta^{33}$ S between ca. – 1.5% and 0%; Jamieson et al. 2013) trapped as pore waters in supracrustal rocks (Sharman et al. 2015; Beaudoin and Chiaradia 2016) and magmatic sulfur, which could be either transported in magmatic fluids or leached from volcanic rocks ( $\delta^{34}$ S = 0% and  $\Delta^{33}$ S = 0%; Labidi et al. 2013; Fiorentini et al. 2018).

The QTC veins of the VVF display a consistent nonzero, slightly negative  $\Delta^{33}$ S signature in both Py1 and Py2 in all orebodies ( $\Delta^{33}$ S =  $\pm 0.03\%$  and  $\pm 0.08\%$ , respectively; Table 3). Moreover, the variable in situ  $\delta^{34}$ S (between -0.4% and 6.3%) and low variance  $\Delta^{33}$ S data (between -0.20% and 0.01%; Fig. 7; Table 2) are in good agreement with high-precision, bulk  $\delta^{34}$ S data (ranging between 0.2% and 5.9%; Fig. 7; Table 2) and  $\Delta^{33}$ S data (ranging between -0.07% and 0%). However, fluid mixing as gold decomplexation mechanism of seawater sulfate trapped in crustal rocks and magmatic sulfur cannot explain the low variance, negative  $\Delta^{33}$ S signature recorded in veinhosted Py2 that contains gold mineralization. Fluid mixing of these two sulfur reservoirs would affect  $\Delta^{33}$ S values (<<-0.10%) and thereby change the  $\Delta^{33}$ S signature during Py2 growth (Figs. 7a and 8). The uncertainty associated with SIMS analyses are too large to be able to see if such a change is present here. Nonetheless, variations in bulk analytical uncertainties are small enough to exclude fluid mixing as a gold decomplexation mechanism. Whereas hydrogen and oxygen isotope compositions recorded in quartz, tourmaline, and carbonate of the VVF indicate fluid mixing



between a deep-seated metamorphic and upper crustal fluids (Beaudoin and Pitre 2005; Beaudoin and Chiaradia 2016), the relatively homogeneous  $\delta^{34}$ S- $\Delta^{33}$ S signature (Fig. 7a), in turn, could be interpreted to indicate that the S budget was dominated by S transported by the metamorphic fluids without significant input of upper crustal sulfur and that fluid mixing was not the driver for gold decomplexation.

#### Fluid boiling and immiscibility

Pressure variations that cause fluid boiling and immiscibility can fractionate  $H_2$  and  $H_2S_{(\alpha)}$  from a hydrothermal fluid, thereby increasing the fluid fO2 (Drummond and Ohmoto 1985; Richards and Kerrich 1993; Wilkinson and Johnston 1996; Palin and Xu 2000; Weatherley and Henley 2013; Hutchison et al. 2020). In a hydrothermal system at 300 °C, near-neutral pH, and  $\Sigma S = 0.05$  mol/kg, this shift in fluid  $fO_2$ can result in the destabilization of Au-sulfide complexes and can lead to a tenfold decrease in gold solubility (Roberts 1987; Seward 1989; McKibben and Eldridge 1990). As the SO<sub>4</sub><sup>2-</sup>/H<sub>2</sub>S ratio increases by removal of reduced H<sub>2</sub> and  $H_2S_{(g)}$ ,  $\delta^{34}S$  values will decrease by up to 20% (Ohmoto and Rye 1979), which has been observed in several magmatic-hydrothermal and orogenic gold orebodies (Peterson and Mavrogenes 2014; Hutchison et al. 2020; Sugiono et al. 2022). Moreover, a significant decrease in gold solubility through As-controlled redox reactions, which causes gold precipitation, can lead to a distinct depletion in  $\delta^{34}$ S signatures recorded between pyrite cores and rims (shift in  $\delta^{34}$ S up to -15%; e.g., Sugiono et al. 2022). Another indicator for oxidizing conditions during gold precipitation is hematite wallrock alteration associated with Au-hosting pyrite showing a negative  $\delta^{34}$ S signature, as observed in the Kalgoorlie gold camp (Yilgarn Craton, Australia; Godefroy-Rodríguez et al. 2020; McDivitt et al. 2022).

In contrast, in the greenstone-hosted VVF, there is no documented evidence for hematite wallrock alteration associated with a decrease in  $\delta^{34}$ S values (Figs. 7a and 8). Instead,  $\delta^{34}$ S values increase from Py1 to homogeneous Py2. Only the Pascalis Gold Trend pyrite records a decrease with slightly higher  $\delta^{34}$ S values (Fig. 7a) in Py1 cores ( $\delta^{34}$ S = 5.2%) compared to homogeneous Py2 rims  $(\delta^{34}S = 3.5\%)$ . In general,  $\delta^{34}S$  values increase with increasing distance from the LLCfz (Figs. 1b and 7a). However, this range between orebodies (from -0.4% to 6.3%) might also be the result of local operating processes. For example, orogenic gold systems are known to entrain locally derived sulfur from meta-sedimentary rocks at the site of gold precipitation (Chang et al. 2008). By comparison, meta-volcanic rocks contain low sulfur concentrations (Patten et al. 2020). Nonetheless, local entrainment of pore waters trapped in meta-volcanic rocks can have a major impact on fluid fO<sub>2</sub>, which can lead to differing  $\delta^{34}$ S values of precipitated pyrite and might explain the range of detected  $\delta^{34}$ S values across VVF orebodies (Ohmoto 1972; Ohmoto and Rye 1979; Pasquier et al. 2021).

Py1 contains inclusions of carbonate, tourmaline, chalcopyrite, and minor pyrrhotite in combination with elevated Ni and Co concentrations (Tables 2 and 3). Particularly, Ni and Co are both known to derive from increased solubilities at higher fO<sub>2</sub> conditions (Fougerouse et al. 2016; Jansson and Liu 2020). These inclusions in Py1 cores could imply rapid crystallization related to phase separation (Román et al. 2019). However, in the case of phase separation, smaller nm- to µm-sized, inclusions together with low Ni and Co concentrations (Román et al. 2019) are expected as opposed to several tens of um-large inclusions as well as elevated Ni and Co concentrations recorded in Py1. Moreover, gold inclusions are contained in homogeneous Py2, which lacks textural evidence for phase separation. In the VVF, positive  $\delta^{34}$ S values are in contrast to sanukitoids and intrusion-related gold deposits in the Abitibi subprovince that commonly record a low  $\delta^{34}$ S signature between – 25% and -5%, indicating either a temperature dependent fractionation or high fluid fO<sub>2</sub> conditions associated with gold mineralization (Hastie et al. 2023). Therefore, fluid boiling and immiscibility leading to an increase in fluid  $fO_2$  are not responsible for gold precipitation in the VVF.

#### Fluid-rock reactions

The Fe-oxide inclusions in Py1 and homogeneous texture in Py2, combined with the increase in  $\delta^{34}$ S values of up to +3.0% from early Py1 to Py2 (Figs. 4, 6 and 7), suggest that the removal of reduced, light sulfur, with low  $\delta^{34}$ S, from a hydrothermal fluid (i.e., fluid desulfidation; Fig. 9a-b) in a reducing environment led to destabilization of Au-sulfide complexes (Seward 1989; McKibben and Eldridge 1990). Fluid desulfidation-wallrock sulfidation has been proposed to remove sulfur from a hydrothermal fluid that ascends through volcanic rocks (e.g., Goldfarb et al. 2005; Robert et al. 2005; Bi et al. 2011; Ward et al. 2017; Jian et al. 2021; Petrella et al. 2021). The reduced sulfur reacts with Fe-bearing minerals common in greenstone rocks (Phillips 1986; Groves et al. 1998, 2000; Goldfarb et al. 2005; Ward et al. 2017). Such minerals that contain reduced iron (e.g., Ferich oxides, carbonates, silicates) either are hosted in igneous wallrock assemblages or occur as a product of wallrock alteration in orogenic gold vein alteration halos. Therefore, Fe-bearing host rock mineral assemblages can significantly enhance fluid desulfidation (i.e., removal of Au-sulfide complexes from a hydrothermal fluid) and, in turn, facilitate wallrock sulfidation (i.e., deposition of sulfides and gold).

The wallrocks of orogenic gold systems in the VVF comprise various intrusive bodies (Fig. 1b), which have all been metamorphosed to regional greenschist facies. These



wallrocks typically contain an igneous assemblage composed to varying proportions of plagioclase, quartz, alkali feldspar, biotite, hornblende and Fe-bearing minerals, particularly ilmenite, titanomagnetite, and magnetite (Fig. 4e–f; Robert and Brown 1986a, b; Groves et al. 1998, 2000; Goldfarb et al. 2005; Rezeau et al. 2017; Dubé 2018; Daver et al. 2020). During fluid-rock reactions leading to wallrock sulfidation (Eqs. 1 and 2), native gold can be precipitated during pyrite growth (Fig. 10a; Reich et al. 2005; Pokrovski et al. 2019).

$$FeTiO_{3(ilmenite)} + 2Au(HS)_{2}^{-} + 2H^{+} = FeS_{2(pyrite)}$$

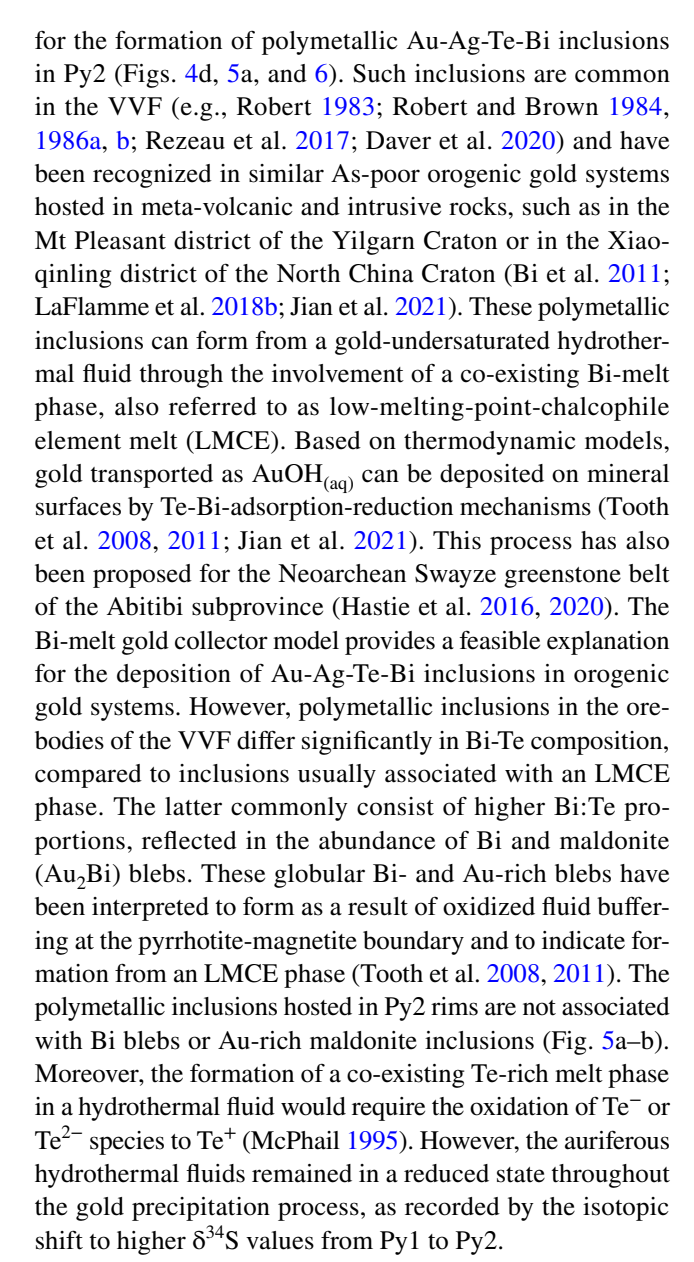
$$+ 2Au_{(gold)} + TiO_{2(rutile)} + 2H_{2}S + H_{2}O$$
(1)

$$Fe_{3}O_{4(\text{magnetite})} + 3Au(HS)_{2}^{-} + 3H^{+} = 3FeS_{2(\text{pyrite})} + 3Au_{(\text{gold})} + 4H_{2}O + \frac{1}{2}H_{2}$$
(2)

This, together with an isotopic shift to higher  $\delta^{34}$ S values, suggests that fluid desulfidation not only decreases  $fS_2$  through the removal of sulfur but also induces a small decrease in fluid fO<sub>2</sub> during Py2 growth (Fig. 9a). Based on an isotopic shift to lower  $\delta^{34}$ S values from early pyrrhotite to late arsenopyrite, Petrella et al. (2021) showed that in orogenic gold systems formed by wallrock sulfidation in As-rich meta-sedimentary rocks, an increase in fluid fO2 would be expected. However, the systematic isotopic shift to higher δ<sup>34</sup>S values between Py1 and Py2 of the VVF, together with native gold and polymetallic Au-Ag-Bi-Te inclusions that are unrelated to zoned areas in Py2 (Fig. 6) with minor and trace concentrations of Ni, Co, or As (Tables 2 and 3), supports a decrease in fluid fO2 for orogenic gold systems formed in As-poor meta-volcanic rocks by sulfidation of Ferich oxides (c.f., Palin and Xu 2000). Daver et al. (2020) document barite and hematite in the VVF that are associated with texturally early pyrite, which support a phase of early pyrite formation under oxidized conditions followed by pyrite growth in more reducing conditions. This implies that pervasive, local fluid-rock interactions, particularly the replacement of Fe-bearing oxides in wallrocks and slivers of wallrocks within veins (Fig. 4b-f; Eqs. 1 and 2), is a main driver to precipitate Py1 and Py2. Subsequent gold precipitation in pyrite is a result of a decrease in gold solubility most likely triggered by intrinsic temperature-pressure fluctuations during wallrock sulfidation in a reducing environment (Fig. 9b; Ohmoto and Rye 1979; Phillips 1986; Palin and Xu 2000; Evans et al. 2006; Ward et al. 2017; Ord and Hobbs 2018; Román et al. 2019).

# Wallrock sulfidation drives Au-Ag-Te-Bi inclusion formation

Whereas decreases in fluid  $fO_2$  and  $fS_2$  explain the precipitation of native gold in Py1 and Py2, they fail to account



Fluid desulfidation under reducing conditions would be consistent with aqueous transport of reduced Te-species (Zhang and Spry 1994; Keith et al. 2018). Based on telluride mineral stability, the abundance of calaverite (AuTe<sub>2</sub>) over petzite (Ag<sub>3</sub>AuTe<sub>2</sub>) and hessite (Ag<sub>2</sub>Te), also recorded by Rezeau et al. (2017) and Daver et al. (2020), in combination with higher  $\delta^{34}$ S values of Py2 suggests that telluride-gold formation likely depended on a coupled decrease of  $fTe_2$ and  $fS_2$  of the hydrothermal fluid (Figs. 10b and 11a-b). Under neutral to alkaline pH, low salinity, high temperature  $(350 \pm 50 \text{ °C})$ , and generally low  $fO_2$  hydrothermal fluids, comparable to those recorded in many Neoarchean orogenic gold systems, Te solubility will decrease under increasingly reduced conditions. The decrease in fluid fO2, associated with a decrease in  $fS_2$ , in the pyrite stability field, induces a drop in fluid fTe<sub>2</sub> and results in telluride deposition (Afifi



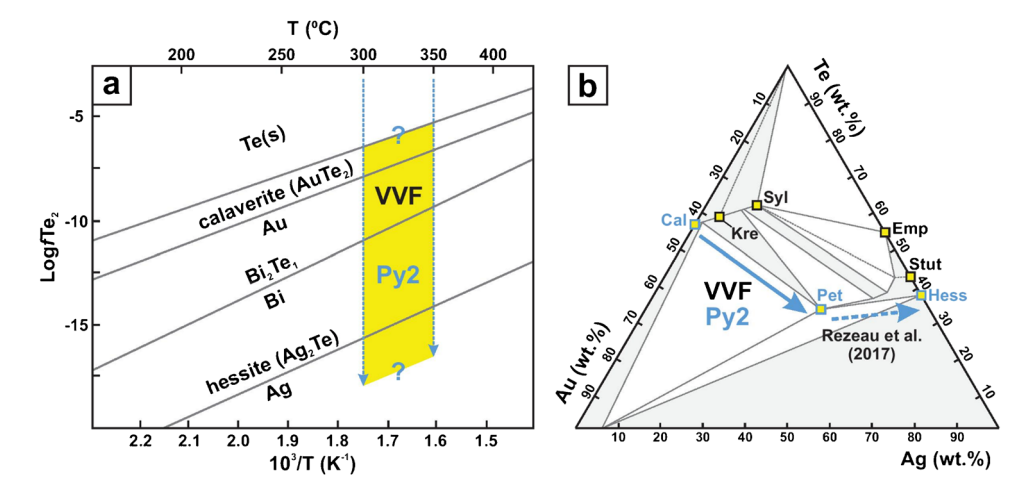


Fig. 11 a A  $\log/\text{Te}_2$ -temperature diagram showing major telluride mineral formation during Py2 growth, related to decreasing  $f\text{Te}_2$  activity in the orogenic gold systems of the VVF. Afifi et al. (1988a, b) Modified from Afifi et al. (1988b). b Ternary Au-Ag-Te diagram showing major telluride mineral compositions (<300 °C) and hydrothermal fluid evolution of the VVF as well as increasingly Ag-rich

tellurides, including hessite, as described by Rezeau et al. (2017) in quartz-tourmaline-carbonate veins of the VVF. Modified after Zhang and Spry (1994), based on data from Markham (1960), Cabri (1965), Legendre et al. (1980), and . Cal=calaverite; Emp=empressite; Hess=hessite; Kre=krennerite; VVF=Val-d'Or Vein Field; Pet=petztite; Stut=stuetzite; Syl=sylvanite

et al. 1988a, b; Zhang and Spry 1994; Cooke and McPhail 2001; Cook et al. 2009; Grundler et al. 2013; Gao et al. 2017; Keith et al. 2018). At approximately 300 °C (Fig. 11a–b), this decrease in fTe $_2$  leads to precipitation of calaverite and evolved towards increasingly Ag-bearing tellurides, such as petztite (Figs. 10b and 11a–b). Therefore, these phases were incorporated into homogeneous Py2 rims and formed polymetallic Au-Ag-Te-Bi inclusions with different Au:Ag proportions, as a result of coupled decreases in fO $_2$ , fS $_2$ , and fTe $_2$  of the hydrothermal fluid (Figs. 9, 10, and 11).

# **Conclusions**

Pyrite hosted within QTC vein orebodies (Goldex, Triangle, Plug #4, Pascalis Gold Trend, Beaufor) of the VVF records a minor ubiquitous shift in  $\delta^{34}$ S values of up to +3.0% from lighter porous core domains (Py1) to heavier homogeneous rims (Py2) and shows a slightly negative  $\Delta^{33}$ S signature, ranging between – 0.20% and 0.01%. Py2 contains most of the associated native gold and polymetallic inclusions (Au-Ag-Te-Bi). The increase in  $\delta^{34}$ S values, combined with, in general, low concentrations in Co and Ni in Py1 cores (<<10,000 ppm), reflects a steady  $fO_2$  and  $fS_2$  decrease. This decrease also led to deposition of Co and Ni in Py1 core domains, as well as the association of texturally-late pyrrhotite with Py2 and the removal of gold-sulfide complexes from the hydrothermal fluid. Our data suggest that a homogeneous fluid reservoir introduced gold-sulfide complexes and that pervasive fluid desulfidation-wallrock sulfidation reactions were

a key mechanism that led to the growth of homogeneous Au-bearing Py2 rims, particularly at the expense of ilmenite, titanomagnetite, and magnetite contained in wallrocks and wallrock slivers within QTC veins. A decrease in the activity of reduced sulfur species drives Au-bearing pyrite precipitation. This reaction is associated with an overall decrease in fO<sub>2</sub> within the pyrite stability field, which, in turn, is responsible for a steady decrease in fTe<sub>2</sub>. This decrease initially precipitated calaverite and upon further decrease in fTe<sub>2</sub> evolved towards increasingly Ag-bearing telluride formation, such as petztite, in Py2 rims. Arsenic contents in As-poor porous Py1 cores (all  $\leq$  67 ppm) and homogeneous Py2 rims ( $\leq$  550 ppm) limit the formation of lattice-bound gold and favor inclusion-hosted gold (Py1, Py1b  $\leq$  30 ppm, and Py2  $\leq$  1250 ppm). The absence of lattice-bound gold, notoriously associated with orogenic gold systems in As-rich rocks, suggests that the VVF presents a prime example for an orogenic gold system that formed in a generally reducing, As-poor (< 0.1 wt%) Archean greenstone belt by fluid-wallrock sulfidation reactions.

**Supplementary Information** The online version contains supplementary material available at https://doi.org/10.1007/s00126-024-01247-6.

Acknowledgements We appreciate financial support for this study by the Canada First Research Excellence Fund Metal Earth project (MERC-ME-2023-37). C.L. acknowledges support from the Canada Research Chair Program. The authors greatly appreciate feedback from K. Kelley, M. Fayek and in particular P. Mercier-Langevin, whose comments helped to significantly improve the state of this manuscript. M.H. greatly thanks at Université Laval M. Choquette, S. Coté, E. Rousseau, at Canadian Malartic Corp. N. Houle, M. Bilodeau, at Agnico Eagle Mines Ltd. R. Morel, J.A. Marcotte, D. Yergeau, at Eldorado



Gold Corp. J. Thelland, É. Gagnon, M. Le Bacq, B. Gagnon and at Probe Metals Inc. M. Gagnon and B. Beh to accommodate the project, micro-analytical work and for logistical support. B. Wing is thanked for bulk multiple sulfur isotope analyses, and M. Aleshin is thanked for his analytical support during the acquisition of in situ sulfur isotope analyses by SIMS. The authors acknowledge the facilities and the scientific and technical assistance of Microscopy Australia at the Centre for Microscopy, Characterisation & Analysis, The University of Western Australia, a facility funded by the University, State, and Commonwealth Governments.

#### **Declarations**

**Competing interests** The authors declare no competing interests.

#### References

- Afifi AM, Kelly WC, Essene EJ (1988a) Phase relations among tellurides, sulfides, and oxides: I. Thermochemical data and calculated equilibria. Econ Geol 83:377–394. https://doi.org/10.2113/gsecongeo.83.2.377
- Afifi AM, Kelly WC, Essene EJ (1988b) Phase relations among tellurides, sulfides, and oxides: II. Applications to telluride-bearing ore deposits. Econ Geol 83:395–404. https://doi.org/10.2113/gsecongeo.83.2.395
- Ayer JA, Thurston PC, Bateman R, Dubé B, Gibson HL, Hamilton MA, Hathway B, Hocker SM, Houlé MG, Hudak G, Ispolatov VO, Lafrance B, Lesher CM, MacDonald PJ, Péloquin AS, Piercey SJ, Reed LE, Thompson PH (2005) Overview of results from the greenstone architecture project: Discover Abitibi initiative. Ontario Geological Survey Open File Report 6154, pp 146. http://www.geologyontario.mndm.gov.on.ca/mndmfiles/pub/data/records/OFR6154.html
- Barré G, Thomassot É, Michels R, Cartigny P, Strzerzynski P, Truche L (2021) Multiple sulfur isotopes signature of thermochemical sulfate reduction (TSR): Insights from Alpine Triassic evaporites. Earth Planet Sci Lett 576:117231. https://doi.org/10.1016/j.epsl.2021.117231
- Bateman R, Hagemann S (2004) Gold mineralisation throughout the 45 Ma of Archean orogenesis: protracted flux of gold in the Golden Mile, Yilgarn craton, Western Australia. Miner Deposita 39:536–559. https://doi.org/10.1007/s00126-004-0431-2
- Beaudoin G, Pitre D (2005) Stable isotope geochemistry of the Archean Val-d'Or (Canada) orogenic gold vein field. Miner Deposita 40:59–75. https://doi-org.acces.bibl.ulaval.ca/https://doi.org/10.1007/s00126-005-0474-z
- Beaudoin G, Chiaradia M (2016) Fluid mixing in orogenic gold deposits: evidence from the H-O-Sr isotope composition of the Vald'Or vein field (Abitibi, Canada). Chem Geol 438:7–18. https://doi.org/10.1016/j.chemgeo.2016.05.009
- Bedeaux P, Pilote P, Daigneault R, Rafini S (2017) Synthesis of the structural evolution and associated gold mineralization of the Cadillac fault, Abitibi, Canada. Ore Geol Rev 82:49–69. https://doi.org/10.1016/j.oregeorev.2016.11.029
- Bi S-J, Li J-W, Zhou M-F, Li Z-K (2011) Gold distribution in Asdeficient pyrite and telluride mineralogy of the Yangzhaiyu gold deposit, Xiaoqinling district, southern North China craton. Miner Deposita 46:925–941. https://doi.org/10.1007/ s00126-011-0359-2
- Bierlein FP, Groves DI, Goldfarb RJ, Dubé B (2006) Lithospheric controls on the formation of provinces hosting giant orogenic gold

- deposits. Miner Deposita 40:874–886. https://doi.org/10.1007/s00126-005-0046-2
- Bleeker W (2015) Synorogenic gold mineralization in granite-greenstone terranes: the deep connection between extension, major faults, synorogenic clastic basins, magmatism, thrust inversion, and long-term preservation. Target Geosci Initiat 4:25–47. https://doi.org/10.4095/296624
- Cabri LJ (1965) Phase relations in the Au-Ag-Te system and their mineralogical significance. Econ Geol 60:1569–1606. https://doi.org/10.2113/gsecongeo.60.8.1569
- Cameron EM, Hattori K (1987) Archean gold mineralisation and oxidised hydrothermal fluids. Econ Geol 82:1177–1191. https://doi.org/10.2113/gsecongeo.82.5.1177
- Camiré GE, Laflèche MR, Ludden JN (1993) Archean metasedimentary rocks from the northwestern Pontiac subprovince of the Canadian shield: Chemical characterization, weathering and modelling of the source areas. Precam Res 62:285–305. https://doi.org/10.1016/0301-9268(93)90026-X
- Caruso S, Fiorentini ML, Champion DC, Lu Y, Ueno Y, Smithies RH (2022) Sulfur isotope systematics of granitoids from the Yilgarn Craton sheds new light on the fluid reservoirs of Neoarchean orogenic gold deposits. Geochim Cosmochim Acta 326:199–213. https://doi.org/10.1016/j.gca.2022.03.023
- Chang Z, Large RR, Maslennikov V (2008) Sulfur isotopes in sediment-hosted orogenic gold deposits: evidence for an early timing and seawater sulfur source. Geology 36(12):971–974. https://doi.org/10.1130/G25001A.1
- Chown EH, Harrap R, Moukhsil A (2002) The role of granitic intrusions in the evolution of the Abitibi belt, Canada. Precam Res 115:291–310. https://doi.org/10.1016/S0301-9268(02)00013-X
- Colvine AC (1989) An empirical model for the formation of Archean gold deposits: products of final cratonization of the Superior Province, Canada. In: Keays RR, Ramsay WRH, Groves DI (eds) The geology of gold deposits: The perspective in 1988: Economic Geology, Monograph 6, pp 37–53. https://doi.org/10.5382/Mono.06.03
- Condie KC (2000) Episodic continental growth models: afterthoughts and extensions. Tectonoph 322:153–162. https://doi.org/10.1016/ S0040-1951(00)00061-5
- Cook NJ, Ciobanu CL, Spry PG, Voudouris P (2009) And the participants of IGCP-486, understanding gold-(silver)-telluride-(selenide) mineral deposits. Episode 32:249–263. https://doi.org/10.18814/epiiugs/2009/v32i4/002
- Cooke DR, McPhail DC (2001) Epithermal Au-Ag-Te mineralization, Acupan, Baguio district, Philippines: Numerical simulations of mineral deposition. Econ Geol 96:109–131. https://doi.org/10. 2113/gsecongeo.96.1.109
- Corfu F (1993) The evolution of the southern Abitibi greenstone belt in light of precise U-Pb geochronology. Econ Geol 88:1323–1340. https://doi.org/10.2113/gsecongeo.88.6.1323
- Corfu F, Jackson SL, Sutcliffe H (1991) U-Pb ages and tectonic significance of late Archean alkalic magmatism and nonmarine sedimentation: Timiskaming group, southern Abitibi belt, Ontario. Can J Earth Sci 28:489–503. https://doi.org/10.1139/e91-043
- Cox SF (2016) Injection-driven swarm seismicity and permeability enhancement: implications for the dynamics of hydrothermal ore systems in high fluid-flux, overpressured faulting regimes. Econ Geol 111:559–587, https://doi.org/10.2113/econgeo.111.3.559
- Daigneault R, Mueller WU, Chown EH (2002) Oblique Archean subduction: accretion and exhumation of an oceanic arc during dextral transpression, Southern Volcanic Zone, Abitibi subprovince Canada. Precam Res 115:261–290. https://doi.org/10.1016/S0301-9268(02)00012-8
- Daver L, Jébrak M, Beaudoin G, Trumbull RB (2020) Three-stage formation of greenstone-hosted orogenic gold deposits in the Val-d'Or mining district, Abitibi, Canada: Evidence from pyrite



- and tourmaline. Ore Geol Rev 120:103449. https://doi.org/10.1016/j.oregeorev.2020.103449
- David J (2019) Datations U-Pb dans les provinces du Supérieur et de Churchill effectuées au GEOTOP en 2014–2015. Québec Ministère des Ressources Naturelles, MB 2019–03, pp 22. https://gq.mines.gouv.qc.ca/documents/EXAMINE/MB201903/ MB201903RAP001.pdf
- Davis DW (2021) Rapport sur les datations U-Pb de roches du Québec 2019–2020. Québec Ministère des Ressources Naturelles, MB 2021–03, pp 190. https://gq.mines.gouv.qc.ca/documents/EXAMINE/MB202103/MB202103RAP001.pdf
- Davis WJ, Machado N, Gariépy C, Sawyer EW, Benn K (1994) U-Pb geochronology of the geochronology of the Opatica tonalite-gneiss belt and its relationship to the Abitibi greenstone belt, Superior province, Quebec. Can J Earth Sci 32:113–127. https://doi.org/10.1139/e95-010
- De Souza S, Dubé B, McNicoll VJ, Dupuis C, Mercier-Langevin P, Creaser RA, Kjarsgaard IM (2017) Geology and hydrothermal alteration of the world-class Canadian Malartic gold deposit: genesis of an Archean stockwork-disseminated gold deposit in the Abitibi Greenstone Belt, Québec. Rev Econ Geol 19:263–291. https://doi.org/10.5382/Rev.19.09
- Dimroth E, Cousineau P, Leduc M, Sanschagrin Y (1978) Structure and organization of Archean subaqueous basalt flows, Rouyn-Noranda area, Quebec, Canada. Can J Earth Sci 15:902–918. https://doi.org/10.1139/e78-101
- Dimroth E, Imreh L, Goulet N, Rocheleau M (1983) Evolution of the south-central segment of the Archean Abitibi Belt, Quebec, Part II: Tectonic evolution and geomechanical model. Can J Earth Sci 20:1355–1373. https://doi.org/10.1139/e83-124
- Drummond SE, Ohmoto H (1985) Chemical evolution and mineral deposition in boiling hydrothermal systems. Econ Geol 80:126– 147. https://doi.org/10.2113/gsecongeo.80.1.126
- Dubé B, Gosselin P (2007) Greenstone-hosted quartz-carbonate vein deposits. In: Goodfellow WD (ed) Mineral deposits of Canada: A synthesis of major deposit-types, district metallogeny, the evolution of geological provinces, and exploration methods: Geological Association of Canada, Mineral Deposit Division, Special Publication no. 5, pp 46–73
- Dubé B, Mercier-Langevin P (2020) Gold deposits of the Archean Abitibi Greenstone Belt, Canada. Econ Geol Spec Pub 23:669– 708. https://doi.org/10.5382/SP.23
- Dubé B, Gosselin P, Mercier-Langevin P, Hannington M, Galley A (2007) Gold-rich volcanogenic massive sulphide deposits of Canada: A synthesis of major deposit-types, district metallogeny, the evolution of geological provinces, and exploration methods: Geological Association of Canada, Mineral Deposits Division, Special Publication no. 5, pp 75–94. https://app.ingemmet.gob.pe/biblioteca/pdf/Econ-46.pdf
- Dubé B, Mercier-Langevin P, Ayer J, Pilote J-L, Monecke T (2020) Gold deposits of the world-class Timmins-Porcupine Camp, Abitibi greenstone belt, Canada. Econ Geol Spec Pub 23:53–80. https://doi.org/10.5382/SP.23.03
- Dubé J (2018) Caractérisation métallogenique et structurale de la minéralisation aurifère des gisements Trangle et Cheminée No. 4, Val-d'Or, Abitibi, Québec: Université du Québec à Chicoutimi, Chicoutimi, Québec, unpublished MSc thesis, pp 258. https://constellation.uqac.ca/4695/1/DubxE9\_uqac\_0862N\_ 10483.pdf
- Ducharme Y, Stevenson RK, Machado N (1997) Sm-Nd geochemistry and U-Pb geochronology of the Preissac and Lamotte leucogranites, Abitibi Subprovince. Can J Earth Sci 34(8):1059–1071. https://doi.org/10.1139/e17-086
- Evans KA, Phillips GN, Powell R (2006) Rock-buffering of auriferous fluids in altered rocks associated with the Golden milestyle mineralization, Kalgoorlie gold field, Western Australia.

- Econ Geol 101:805-817. https://doi.org/10.2113/gsecongeo. 101.4.805
- Feng R, Kerrich R (1991) Single zircon age constraints on the tectonic juxtaposition of the Archean Abitibi greenstone belt and Pontiac subprovince, Quebec, Canada. Geochim Cosmochim Acta 55:3437–3441. https://doi.org/10.1016/0016-7037(91) 90502-V
- Feng R, Kerrich R, McBride S, Farrar E (1992) <sup>40</sup>Ar/<sup>39</sup>Ar constraints on the thermal history of the Archean Abitibi greenstone belt and Pontiac subprovince: Implications for terrane collision, differential uplift, and overprinting of gold deposits. Can J Earth Sci 29:1389–1411. https://doi.org/10.1139/e92-112
- Ferguson SA, Buffam BSW, Carter OF, Griffis AT, Holmes TC, Hurst ME, Jones WA, Lane HC, Longley CS (1968) Geology and ore deposits of Tisdale Township, District of Cochrane. Ontario Geological Survey R058
- Fiorentini ML, LaFlamme C, Denyszyn S, Mole D, Maas R, Locmelis M, Caruso S, Bui TH (2018) Post-collisional alkaline magmatism as gateway for metal and sulfur enrichment of the continental lower crust. Geochim Cosmochim Acta 223:175– 197. https://doi.org/10.1016/j.gca.2017.11.009
- Fougerouse D, Mickelthwaite S, Tomkins AG, Mei Y, Kilburn M, Guagliardo P, Fisher LA, Halfpenny A, Gee M, Paterson D, Howard DL (2016) Gold remobilisation and formation of high grade ore shoots driven by dissolution-reprecipitation replacement and Ni substitution into auriferous arsenopyrite. Geochim Cosmochim Acta 178:143–159. https://doi-org.acces.bibl.ulaval.ca/https://doi.org/10.1016/j.gca.2016.01.040
- Gao S, Xu H, Li SX, Santosh M, Zhang D, Yang L, Quan S (2017) Hydrothermal alteration and ore-forming fluids associated with gold-tellurium mineralization in the Dongping gold deposit, China. Ore Geol Rev 80:166–184. https://doi.org/10.1016/j.oregeorev.2016.06.023
- Godefroy-Rodríguez M, Hagemann S, LaFlamme C, Fiorentini M (2020) The multiple sulfur isotope architecture of the Golden mile and Mount Charlotte deposits, Western Australia. Miner Deposita 55:797–822. https://doi.org/10.1007/s00126-018-0828-y
- Goldfarb RJ, Groves DI, Gardoll S (2001) Orogenic gold and geologic time: A global synthesis. Ore Geol Rev 18:1–75. https://doi.org/ 10.1016/S0169-1368(01)00016-6
- Goldfarb RJ, Baker T, Dubé B, Groves DI, Hart CJR, Gosselin P (2005) Distribution, character, and genesis of gold deposits in metamorphic terranes. Econ Geol 100<sup>th</sup> Anni Vol, pp 407–450. https://doi. org/10.5382/AV100.14
- Goldfarb RJ, Groves DI (2015) Orogenic gold: Common or evolving fluid and metal sources through time. Lithos 233:2–26. https://doi.org/10.1016/j.lithos.2015.07.011
- Gosselin P, Dubé B (2005) Gold deposits of the world: distribution, geological parameters and gold content. Geological Survey of Canada Open File 4895, pp 271.https://doi.org/10.4095/220379
- Groves DI (1993) The crustal continuum model for late-Archean lodegold deposits of the Yilgarn Block, Western Australia. Miner Deposita 28:366–374. https://doi.org/10.1007/BF02431596
- Groves DI (2003) Gold deposits in metamorphic belts: overview of current understanding, outstanding problems, future research and exploration significance. Econ Geol 98:1–29. https://doi.org/10.2113/98.1.1
- Groves DI, Santosh M (2016) The giant Jiaodong gold province: The key to a unified model for orogenic gold deposits? Geosci Front 7:409–417. https://doi.org/10.1016/j.gsf.2015.08.002
- Groves DI, Goldfarb RJ, Gebre-Mariam M, Hagemann SG, Robert F (1998) Orogenic gold deposits: A proposed classification in the context of their crustal distribution and relationship to other gold deposit types. Ore Geol Rev 13:7–27. https://doi.org/10.1016/S0169-1368(97)00012-7



- Groves DI, Goldfarb RJ, Knox-Robinson CM, Ojala J, Gardoll S, Yun GY, Holyland P (2000) Late-kinematic timing of orogenic gold deposits and significance for computer-based exploration techniques with emphasis on the Yilgarn Block, Western Australia.

  Ore Geol Rev 17:1–38. https://doi.org/10.1016/S0169-1368(00) 00002-0
- Groves DI, Condie KC, Goldfarb RJ, Hronsky JMA, Vielreicher RM (2005) Secular changes in global tectonic processes and their influence on the temporal distribution of gold-bearing mineral deposits. Econ Geol 100<sup>th</sup> Anniv. Vol., 203–224. https://doi.org/ 10.2113/gsecongeo.100.2.203
- Grundler PV, Brugger J, Etschmann BE, Helm L, Liu WH, Spry PG, Tian Y, Testemale D, Pring A (2013) Speciation of aqueous tellurium (IV) in hydrothermal solutions and vapors and the role of oxidized tellurium species in Te transport and gold deposition. Geochim Cosmochim Acta 120:298–325. https://doi.org/10.1016/j.gca.2013.06.009
- Guillong M, Hametner K, Reusser E, Wilson SA, Günther D (2005)
  Preliminary characterisation of new glass reference materials
  (GSA-1G, GSC-1G, GSD-1G and GSE-1G) by laser ablationinductively coupled plasma-mass spectrometry using 193
  nm, 213 nm and 266 nm wavelengths. Geostand Geoanal Res
  29(3):315–331. https://doi.org/10.1111/j.1751-908X.2005.tb009
  03.x
- Hastie ECG, Kontak DJ, Lafrance B (2016) Update on activities related to a gold metallogenic study of the southern Swayze greenstone belt: Ontario Geological Survey Open File Report 6323, pp 8–1–8–10. http://www.geologyontario.mndmf.gov.on.ca/mndmaccess/mndm\_dir.asp?type=pub&id=OFR6323
- Hastie ECG, Kontak DJ, Lafrance B (2020) Gold remobilization: insights from gold deposits in the Archean Swayze greenstone belt, Abitibi subprovince, Canada. Econ Geol 115(2):241–277. https://doi.org/10.5382/econgeo.4709
- Hastie ECG, Kontak DJ, Lafrance B, Petrus JA, Sharpe R, Fayek M (2023) Evaluating geochemical discriminants in Archean gold deposits: A superior province perspective with an emphasis on the Abitibi greenstone belt. Econ Geol 118(1):123–155. https:// doi.org/10.5382/econgeo.4979
- Helt KM (2012) The Canadian Malartic deposit: An example of oxidized, intrusion-related gold mineralization in the Abitibi greenstone belt, Québec, Canada: McGill University, Montréal, Québec, unpublished MSc thesis, pp 171. https://escholarship.mcgill.ca/concern/theses/6395wc29r
- Helt KM, Williams-Jones AE, Clark JR, Wing BA, Wares RP (2014) Constraints on the genesis of the archean oxidized, intrusionrelated Canadian Malartic gold deposit, Quebec, Canada. Econ Geol 109:719–735. https://doi.org/10.2113/econgeo.109.3.713
- Herzog M, LaFlamme C, Beaudoin G, Marsh J, Guilmette C (2023) U-Pb vein xenotime geochronology constraints on timing and longevity of orogenic gold mineralization in the Malartic-Vald'Or Camp, Abitibi subprovince, Canada. Miner Deposita 58:105–133. https://doi.org/10.1007/s00126-022-01131-1
- Hodgson CJ (1993) Mesothermal lode-gold deposits. In: Kirkham RV, Sinclair WD, Thorpe RI, Duke JM (eds) Mineral deposits modeling: Geological Association of Canada, Special Paper 40, pp 635–678
- Hodgson CJ, Hamilton JV (1989) Gold mineralization in the Abitibi greenstone belt: end-stage result of Archean collisional tectonics? In: Keays RR, Ramsay WRH, Groves DI (eds) The geology of gold deposits: The perspective in 1988: Economic Geology, Monograph 6, pp 86–100. https://doi.org/10.5382/Mono.06.06
- Hodkiewicz PF, Groves DI, Davidson GJ, Weinberg RF, Hagemann SG (2009) Influence of structural setting on sulphur isotopes in archean orogenic gold deposits, eastern Goldfields Province, Yilgarn, Western Australia. Miner Deposita 44:129–150. https:// doi.org/10.1007/s00126-008-0211-5

- Hutchison W, Finch AA, Boyce AJ (2020) The sulfur isotope evolution of magmatic-hydrothermal fluids: Insights into ore-forming processes. Geochim Cosmochim Acta 288:176–198. https://doi.org/10.1016/j.gca.2020.07.042
- Hyde RS (1980) Sedimentary facies in the Archean Timiskaming Group and their tectonic implications, Abitibi greenstone belt, northeastern Ontario, Canada. Precam Res 12:161–195. https://doi.org/10.1016/0301-9268(80)90028-5
- Imreh L (1984) Sillon de La Motte-Vassan et son avant-pays meridional: Synthèse volcanologique, lithostratigraphique et gîtologique. Ministère de l'Énergie et des Ressources du Québec, report MM 82–04, pp 72. https://gq.mines.gouv.qc.ca/docum ents/EXAMINE/MM8204/MM8204.pdf
- Jamieson JW, Wing BA, Hannington MD, Farquhar J (2006) Evaluating isotopic equilibrium among sulfide mineral pairs in Archean ore deposits: case study from the Kidd Creek VMS deposit, Ontario, Canada. Econ Geol 101:1055–1061. https://doi.org/10.2113/ gsecongeo.101.5.1055
- Jamieson JW, Wing BA, Farquhar J, Hannington MD (2013) Neoarchean seawater sulphate concentrations from sulphur isotopes in massive sulphide ore. Nat Geosci 6:61–64. https://doi.org/10. 1038/ngeo1647
- Jansson NF, Liu W (2020) Controls on cobalt and nickel distribution in hydrothermal sulphide deposits in Bergslagen, Sweden – constraints from solubility modelling. GFF 142(2):87–95. https:// doi.org/10.1080/11035897.2020.1751270
- Jian W, Mao J, Lehmann B, Cook NJ, Xie G, Liu P, Duan C, Alles J, Niu Z (2021) Au-Ag-Te-rich melt inclusions in hydrothermal gold-quartz veins, Xiaoqinling lode gold district, Central China. Econ Geol 116(5):1239–1248. https://doi.org/10.5382/econgeo. 4811
- Jochum KP, Nohl K, Herwig K, Lammel E, Stoll B, Hofmann AW (2005) GeoReM: A new geochemical database for reference materials and isotopic standards. Geostand Geoanalytical Res 29(3):333–338. https://doi.org/10.1111/j.1751-908X.2005.tb009 04.x
- Keith M, Smith DJ, Jenkin GRT, Holwell DA, Dye MD (2018) A review of Te and Se systematics in hydrothermal pyrite from precious metal deposits: Insights into ore-forming processes. Ore Geol Rev 96:269–282. https://doi.org/10.1016/j.oregeorev. 2017.07.023
- Kerrich R, King R (1993) Hydrothermal zircon and baddeleyite in Val-d'Or Archean mesothermal gold deposits: characteristics, compositions, and fluid-inclusion properties, with implications for timing of primary gold mineralization. Can J Earth Sci 30:2334–2351. https://doi.org/10.1139/e93-203
- Kerrich R, Goldfarb R, Groves D, Garvin S (2000) The geodynamics of world-class gold deposits-characteristics, space-time distribution, and origins. Rev Econ Geol 13:501–544. https://doi.org/10. 5382/Rev.13.15
- Labidi J, Cartigny P, Moreira M (2013) Non-chondritic Sulphur isotope composition of the terrestrial mantle. Nature 501:208–211. https://doi.org/10.1038/nature12490
- LaFlamme C, Martin L, Jeon H, Reddy SM, Selvaraja V, Caruso S, Bui TH, Roberts MP, Voute F, Hagemann S, Wacey D, Littman S, Wing B, Fiorentini M, Kilburn MR (2016) In situ sulfur isotope analysis by SIMS of pyrite, chalcopyrite, pyrrhotite, and pentlandite to refine magmatic ore genetic models. Chem Geol 444:1–15. https://doi.org/10.1016/j.chemgeo.2016.09.032
- LaFlamme C, Fiorentini ML, Lindsay MD, Bui TH (2018a) Atmospheric sulfur is recycled to the crystalline continental crust during supercontinent formation. Nat Commun 9(1):1–9. https://doi.org/10.1038/s41467-018-06691-3
- LaFlamme C, Jamieson JW, Fiorentini ML, Thébaud N, Caruso S, Selvaraja V (2018b) Investigating sulfur pathways through the lithosphere by tracing mass independent fractionation of sulfur



- to the Lady Bountiful orogenic gold deposit. Gondwana Res 58:27–38. https://doi.org/10.1016/j.gr.2018.02.005
- LaFlamme C, Sugiono D, Thébaud N, Caruso S, Fiorentini M, Selvaraja V, Jeon H, Voute F, Martin L (2018c) Multiple sulfur isotopes monitor fluid evolution of an Archean orogenic gold deposit. Geochim Cosmochim Acta 222:436–446. https://doi.org/10.1016/j.gca.2017.11.003
- Latulippe M (1966) The relationship of mineralization to precambrian stratigraphy in the Matagami Lake and Val-d'Or districts of Ouébec. Geol Assoc Can 3:21–42
- Legendre B, Souleau C, Hancheng C (1980) Le système ternaire orargent-tellure. Soc Chim Fran Bull 1:197–204
- Lipson R (2014) The promise and perils of porphyry deposits in the future of gold production. SEG Newslet 98(1):14–20. https://doi.org/10.5382/SEGnews.2014-98.fea
- Loucks RR, Mavrogenes JA (1999) Gold solubility in supercritical hydrothermal brines measured in synthetic fluid inclusions. Science 284:2159–2163. https://doi.org/10.1126/science.284. 5423.2159
- Machado N, Philippe S, Gariépy C, David J (1991) Géochronologie U-Pb territoire québécois: Fosses du l'Ungava et Sous-Province de Pontiac. Ministère de l'Énergie et des Ressources du Québec, report, MB 91–07, 50 p.
- Machado N, Gariépy C (1994) Géochronologie U-Pb du territoire québecois, la Sous-province de l'Abitibi, cinquième rapport intérimaire: résultats 1993–1994. Ministère des Ressources naturelles, Québec, internal report, pp 21. https://gq.mines.gouv.qc.ca/documents/examine/GM66921/GM66921.pdf
- Markham NL (1960) Synthetic and natural phases in the system Au-Ag-Te. Econ Geol 55:1148–1178. https://doi.org/10.2113/gsecongeo.55.6.1148
- McCuaig TC, Kerrich R (1998) P-T-t-deformation-fluid characteristics of lode gold deposits: evidence from alteration systematics. Ore Geol Rev 12(6):381–453. https://doi.org/10.1016/S0169-1368(98)80002-4
- McDivitt JA, Hagemann SG, Thébaud N, Martin LAJ, Rankenburg K (2022) Constraints on the structural setting, relative timing, and geochemistry of the Fimiston, Hidden Secret, and Oroya gold-telluride lode types, Kalgoorlie gold camp, Western Australia. Miner Deposita 1:1–24. https://doi.org/10.1007/s00126-021-01077-w
- McKibben MA, Eldridge CS (1990) Radical sulfur isotope zonation of pyrite accompanying boiling and epithermal gold deposition; a SHRIMP study of the Valles Caldera, New Mexico. Econ Geol 85:1917–1925. https://doi.org/10.2113/gsecongeo. 85.8.1917
- McPhail DC (1995) Thermodynamic properties of aqueous tellurium species between 25°C and 350°C. Geochim Cosmochim Acta 59:851–866. https://doi.org/10.1016/0016-7037(94)00353-X
- Mercier-Langevin P, Dubé B, Hannington MD, Davis DW, Lafrance B, Gosselin G (2007) The LaRonde Penna Au-rich volcanogenic massive sulfide deposit, Abitibi greenstone belt, Quebec: Part I. Geology and geochronology. Econ Geol 102(4):585–609. https://doi.org/10.2113/gsecongeo.102.4.585
- Mikucki EJ, Ridley JR (1993) The hydrothermal fluid of Archean lodegold deposits at different metamorphic grades: Compositional constraints from ore and wallrock assemblages. Miner Deposita 28:469–481. https://doi.org/10.1007/BF02431603
- Monecke T, Mercier-Langevin P, Dubé B, Friedman M (2017) Geology of the Abitibi Greenstone Belt: Rev. Econ Geol 19:7–50. https://doi.org/10.5382/Rev.19.01
- Montsion RM, Thurston P, Ayer J (2018) 1:2000000 scale geological compilation of the superior craton legend. https://merc.laurentian.ca/sites/default/files/superiormap\_8x11\_2018.pdf
- Morasse SMRI (1998) Geology, structure and timing of gold mineralization at the Kiena Deposit, Val-d'Or, Québec: Queen's

- University, Kingston, Ontario, unpublished PhD thesis, pp 362. https://www.collectionscanada.gc.ca/obj/s4/f2/dsk2/tape17/PQDD\_0005/NQ31942.pdf
- Morasse S, Wasteneys HA, Cormier M, Helmstaedt H, Mason R (1995) A pre-2686 ma intrusion-related gold deposit at the Kiena Mine, Val d'Or, Québec, southern Abitibi subprovince. Econ Geol 90:1310–1321. https://doi.org/10.2113/gsecongeo.90.5.1310
- Moser DE (1994) The geology and structure of the mid-crustal Wawa gneiss domain: a key to understanding tectonic variation with depth and time in the late Archean Abitibi-Wawa orogeny. Can J Earth Sci 31:1064–1080. https://doi.org/10.1139/e94-096
- Mungall JE, Brenan JM (2014) Partitioning of platinum-group elements and Au between sulfide liquid and basalt of the origins of mantle-crust fractionation of the chalcophile elements. Geochim Cosmochim Acta 125:265–289. https://doi.org/10.1016/j.gca.2013.10.002
- Munger A (2019) Facteurs de contrôle et organisation des filons aurifères orogéniques du gisement de Goldex, Val-d'Or, Québec: Université du Québec à Chicoutimi, Chicoutimi, Québec, unpublished MSc thesis, pp 249. https://constellation.uqac.ca/id/eprint/5234/1/Munger\_uqac\_0862N\_10588.pdf
- Neumayr P, Walshe J, Hagemann S, Peterson K, Roache A, Frikken P, Horn L, Haley S (2008) Oxidized and reduced mineral assemblages in greenstone belt rocks of the At. Ives gold camp, Western Australia: vectors to high-grade ore bodies in Archean gold deposits? Miner Deposita 43:363–371. https://doi.org/10.1007/ s00126-007-0170-2
- Ohmoto H (1972) Systematics of sulfur and carbon isotopes in hydrothermal ore deposits. Econ Geol 67:551–578. https://doi.org/10. 2113/gsecongeo.67.5.551
- Ohmoto H, Rye RO (1979) Isotopes of sulfur and carbon. Geochem Hydroth Ore Dep 509–567
- Ono S, Kaufman AJ, Farquhar J, Sumner DY, Beukes NJ (2009) Lithofacies control on multiple-sulfur isotope records and Neoarchean sulfur cycles. Precam Res 169:58–67. https://doi.org/10.1016/j. precamres.2008.10.013
- Ord A, Hobbs BE (2018) Episodic modes of operation in hydrothermal gold systems: Part I. Deformation, mineral reactions and chaos. Geol Soc Lon Spec Pub 453:121–146. https://doi.org/10.1144/SP453.14
- Palin JM, Xu Y (2000) Gilt by association? Origins of pyritic gold ores in the victory mesothermal gold deposit, Western Australia. Econ Geol 95:1627–1634. https://doi.org/10.2113/gsecongeo. 95.8.1627
- Pasquier V, Bryant RN, Fike DA, Halevy I (2021) Strong local, not global, controls on marine pyrite sulfur isotopes. Sci Adv 7.9:eabb7403. https://doi.org/10.1126/sciadv.abb7403
- Paton C, Hellstrom J, Paul B, Woodhead J, Hergt J (2011) Iolite: Freeware for the visualisation and processing of mass spectrometric data. J Anal Spec 26:2508–2518. https://doi.org/10.1039/C1JA1 0172B
- Patten CGC, Pitcairn IK, Molnár F, Beaudoin G, Guilmette C, Peillod A (2020) Gold mobilization during metamorphic devolatilization of Archean and paleoproterozoic metavolcanic rocks. Geology 48:1110–1114. https://doi.org/10.1130/G47658.1
- Paul B, Petrus J, Savard D, Woodhead J, Hergt J, Greig A, Paton C, Rayner P (2023) Time resolved trace element calibration strategies for LA-ICP-MS. J Anal At Spectrom 38(10):1995–2006. https://doi.org/10.1039/D3JA00037K
- Peterson EC, Mavrogenes JA (2014) Linking high-grade gold mineralization to earthquake-induced fault-valve processes in the Porgera gold deposit, Papua New Guinea. Geology 42(5):383–386. https://doi.org/10.1130/G35286.1
- Petrella L, Thébaud N, Evans K, LaFlamme C, Occhipinti S (2021)

  The role of competitive fluid-rock interaction processes in the



- formation of high-grade gold deposits. Geochim Cosmochim Acta 313:38–54. https://doi.org/10.1016/j.gca.2021.08.024
- Pettke T, Diamond LW, Villa IM (1999) Mesothermal gold veins and metamorphic devolatilization in the northwestern Alps: The temporal link. Geology 27(7):641–644. https://doi.org/10.1130/0091-7613(1999)027%3C0641:MGVAMD%3E2.3.CO;2
- Phillips GN (1986) Geology and alteration in the Golden Mile, Kalgoorlie. Econ Geol 81(4):779–808. https://doi.org/10.2113/ gsecongeo.81.4.779
- Phillips GN, Powell R (2010) Formation of gold deposits: A metamorphic devolatilization model. J Met Geol 28:698–718. https://doi.org/10.1111/j.1525-1314.2010.00887.x
- Piette-Lauzière N, Guilmette C, Bouvier A, Perrouty S, Pilote P, Gaillard N, Lypaczewski P, Linnen RL, Olivo GR (2019) The timing of prograde metamorphism in the Pontiac subprovince, superior craton: implications for Archean geodynamics and gold mineralization. Precam Res 320:111–136. https://doi.org/ 10.1016/j.precamres.2018.10.016
- Pilote P, Mueller WU, Scott CR, Lavoie S (1999) Géologie des formations Val-d'Or, Héva et Jacola Nouvelle interpretation du bloc Malartic: Séminaire d'Information sur la Recherche Géologique, Programme et résumés. Ministère des Ressources naturelles, Québec, DV 99-03, pp 19
- Pilote P, Moorhead J, Mueller W (2000) Partie A. Développement d'un arc volcanique, La region de Val d'Or, ceinture de l'Abitibi: Volcanologie physique et évolution métallogénique. Québec Ministère des Ressources Naturelles, MB 2000–09, pp 20. https://gq.mines.gouv.qc.ca/documents/examine/MB200 009/MB200009.pdf
- Pilote P, Daigneault R, David J, McNicoll V (2015) Architecture of the Malartic, Piché and Cadillac groups and the Cadillac Fault: geological revisions, new dates and interpretations. Ministère de l'Énergie et des Ressources Naturelles, Abstracts of Oral Presentations and Posters, Québec Mines, 2014, pp 37
- Pitcairn IK, Teagle DAH, Craw D, Olivo GR, Kerrich R, Brewer TS (2006) Sources of metals and fluids in orogenic gold deposits: insights from the Otago and Alpine Schists, New Zealand. Econ Geol 101:1525–1546. https://doi.org/10.2113/gsecongeo. 101.8.1525
- Pitcairn IK, Craw D, Teagle DAH (2015) Metabasalts as sources of metals in orogenic gold deposits. Miner Deposita 50:373–390. https://doi.org/10.1007/s00126-014-0547-y
- Pitcairn IK, Leventis N, Beaudoin G, Faure S, Guilmette C, Dubé B (2021) A metasedimentary source of gold in Archean orogenic gold deposits. Geology 49(G48587):1. https://doi.org/10.1130/G48587.1
- Pokrovski GS, Akinfiev NN, Borisova AY, Zotov AV, Kouzmanov K (2014) Gold speciation and transport in geological fluids: insights from experiments and physical-chemical modelling. Geol Soc Lon Spec Pub 402(1):9–70. https://doi.org/10.1144/SP402.4
- Pokrovski GS, Kokh MA, Guillaume D, Borisova AY, Gisquet P, Hazemann J-L, Lahera E, Net WD, Proux O, Testemale D, Haigis V, Jonchière R, Seitsonen AP, Ferlat G, Vuilleumier R, Saitta AM, Boiron M-C, Dubessy J (2015) Sulfur radical species from gold deposits on earth. Proc Nat Acad Sci USA 112(44):13484–13489. https://doi.org/10.1073/pnas.15063 78112
- Pokrovski GS, Kokh MA, Proux O, Hazemann J-L, Bazarkina EF, Testemale D, Escoda C, Boiron M-C, Blanchard M, Aigouy T, Gouy S, de Parseval P, Thibaut M (2019) The nature and partitioning of invisible gold in the pyrite-fluid system. Ore Geol Rev 109:545–563. https://doi.org/10.1016/j.oregeorev. 2019 04 024
- Pokrovski GS, Escoda C, Blanchard M, Testemale D, Hazemann J-L, Gouy S, Kokh MA, Boiron M-C, de Parseval F, Aigouy T,

- Menjot L, de Parseval P, Proux O, Rovezzi M, Béziat D, Salvi S, Kouzmanov K, Bartsch T, Pöttgen R, Doert T (2021) An arsenic-driven pump for invisible gold in hydrothermal systems. Geochem Persp Let 17:39–44. https://doi.org/10.7185/geochemlet. 2112
- Pokrovski GS, Desmaele E, Laskar C, Bazarkina EF, Testemale D, Hazemann J-L, Vuilleumier R, Seitsonen AP, Ferlat G, Saita AM (2022) Gold speciation in hydrothermal fluids revealed by in-situ high energy resolution X-ray absorption spectroscopy. Am Mineral 107:369–376. https://doi.org/10.2138/am-2022-8008
- Poulsen KH (2017) The Larder-Lake Cadillac break and its gold districts. Rev Econ Geol 19:133–167. https://doi.org/10.5382/Rev. 19.05
- Powell WG, Carmichael DM, Hodgson CJ (1995) Conditions and timing of metamorphism in the southern Abitibi greenstone belt, Quebec. Can J Earth Sci 32:787–805. https://doi.org/10.1139/e95-067
- Pyke DR, Naldrett AJ, Eckstrand OR (1973) Archean ultramafic flows in Munro township; Ontario. Geol Soc Am Bull 84:955–978. https://doi.org/10.1130/0016-7606(1973)84%3C955:AUFIMT% 3E2.0.CO;2
- Rehm AG, Jørgensen TRC, Thurston PC, Gibson HL, Lafrance B (2021) Synsedimentary rifting and basaltic-komatiitic volcanism in the Pontiac subprovince, Superior craton (Canada): Implications for Neoarchean geodynamics. Precam Res 362:106204. https://doi.org/10.1016/j.precamres.2021.106204
- Reich M, Kesler SE, Utsunomiya S, Palenik CS, Chryssoulis SL, Ewing RC (2005) Solubility of gold in arsenian pyrite. Geochim Cosmochim Acta 69(11):2781–2796. https://doi.org/10.1016/j. gca.2005.01.011
- Rezeau H, Moritz R, Beaudoin G (2017) Formation of Archean batholith-hosted gold veins at the Lac Herbin deposit, Vald'Or district. Canada: mineralogical and fluid inclusion constraints. Miner Deposita 52.3:421–442. https://doi.org/10.1007/s00126-016-0669-5
- Richards JP, Kerrich R (1993) The Porgera gold mine, Papua New Guinea; Magmatic hydrothermal to epithermal evolution of an alkali-type precious metal deposit. Econ Geol 88(5):1017–1052. https://doi.org/10.2113/gsecongeo.88.5.1017
- Robert F (1983) Etude du mode de mise en place des veines aurifères de la mine Sigma, Val-d'Or, Québec: École Polytechnique, Montréal, Québec, unpublished PhD thesis, pp 295. https://gq.mines.gouv.qc.ca/documents/EXAMINE/TH1096/TH1096.pdf
- Robert F (1989) Internal structure of the Cadillac tectonic zone southeast of Val d'Or, Abitibi greenstone belt, Quebec. Can J Earth Sci 26:2661–2675. https://doi.org/10.1139/e89-226
- Robert F (1990) Structural setting and control of gold-quartz veins of the Val-d'Or area, southeastern Abitibi subprovince: Gold and base metal mineralization in the Abitibi sub-province, Canada, with emphasis of the Quebec segment: Geology Department (Key Centre) and University Extension, the University of Western Australia. Publication No. 24, pp 167-210
- Robert F (1994) Vein field in gold districts: the example of Val-d'Or, southeastern Abitibi subprovince, Quebec: Current Research 1994-C. Geological Survey of Canada, pp 295–302. https://doi.org/10.4095/193837
- Robert F (1997) A preliminary geological model for syenite-associated disseminated gold deposits in the Abitibi belt, Ontario and Quebec: Current Research 1997-C. Geological Survey of Canada, pp 201–210.
- Robert F, Brown AC (1984) Progressive alteration associated with Gold Quartz Veins of the Sigma mine, Abitibi greenstone belt, Quebec. Econ Geol 79:393–399. https://doi.org/10.2113/gsecongeo.79.2.393
- Robert F, Brown AC (1986a) Archean gold-bearing quartz veins at the Sigma mine, Abitibi greenstone belt, Quebec: Part I. Geologic



- relations and formation of the vein system. Econ Geol 81:578–592. https://doi.org/10.2113/gsecongeo.81.3.578
- Robert F, Brown AC (1986b) Archean gold-bearing quartz veins at the Sigma mine, Abitibi greenstone belt, Quebec: Part II. Vein paragenesis and hydrothermal alteration. Econ Geol 81:593–616. https://doi.org/10.2113/gsecongeo.81.3.593
- Robert F, Poulsen KH, Cassidy KF, Hodgson CJ (2005) Gold metallogeny of the Superior and Yilgarn Cratons: Econ Geol 100<sup>th</sup> Anni Vol, pp 1001–1033. https://doi.org/10.5382/AV100.30
- Roberts RG (1987) Ore deposit models #11. Archean lode gold deposits. Geosci Canada 14:37-52
- Román N, Reich M, Leisen M, Morata D, Barra F, Deditius AP (2019) Geochemical and micro-textural fingerprints of boiling in pyrite. Geochim Cosmochim Acta 246:60–85. https://doi.org/10.1016/j.gca.2018.11.034
- Ross PS, Goutier J, Mercier-Langevin P, Dubé B (2011a) Basaltic to andesitic volcaniclastic rocks in the Blake River Group, Abitibi greenstone belt: 1. Mode of emplacement in three areas. Can J Earth Sci 48:728–756. https://doi.org/10.1139/e10-090
- Ross PS, McNicoll V, Goutier J, Mercier-Langevin P, Dubé B (2011b) Basaltic to andesitic volcaniclastic rocks in the Blake River Group, Abitibi greenstone belt: 2. Origin, geochemistry and geochronology. Can J Earth Sci 48:757–777. https://doi.org/10. 1139/e10-102
- Savard D, Bouchard-Boivin B, Barnes S-J, Garbe-Schönberg D (2018) UQAC-FeS: A new series of base metal sulfide quality control reference material for LA-ICP-MS analysis. Proceedings of 10<sup>th</sup> International Conference on the Analysis of Geological and Environmental Materials, pp 8–13
- Savard D, Dare S, Bédard LP, Barnes S-J (2023) A new mapping protocol for laser ablation (with Fast-Funnel) coupled to a time of flight mass spectrometer (LA-FF-ICP-ToF-MS) for the rapid, simultaneous quantification of multiple minerals. Geostand Geoanal Res 47(2):243–265. https://doi.org/10.1111/ggr.12482
- Scott CR, Mueller WU, Pilote P (2002) Physical volcanology, stratigraphy, and lithogeochemistry of an archean volcanic arc: Evolution from plume-related volcanism to arc rifting of SE Abitibi greenstone belt, Val-d'Or, Canada. Precam Res 115:223–260. https://doi.org/10.1016/S0301-9268(02)00011-6
- Selvaraja V, Caruso S, Fiorentini ML, LaFlamme CK, Bui T-H (2017) Atmospheric sulfur in the orogenic gold deposits of the Archean Yilgarn Craton, Australia. Geology 45(8):691–694. https://doi. org/10.1130/G39018.1
- Seward TM (1989) The hydrothermal chemistry of gold and its implications for ore formation: Boiling and conductive cooling as examples. Econ Geol 6:398–404. https://doi.org/10.5382/Mono.
- Sharman ER, Taylor BE, Minarik WG, Dubé B, Wing BA (2015) Sulfur isotope and trace element data from ore sulfides in the Noranda district (Abitibi, Canada): Implications for volcanogenic massive sulfide deposit genesis. Miner Deposita 50:591–606. https://doi.org/10.1007/s00126-014-0559-7
- Shenberger D, Barnes H (1989) Solubility of gold in aqueous sulfide solutions from 150 to 350°C. Geochim Cosmochim Acta 53:269–278. https://doi.org/10.1016/0016-7037(89)90379-7
- Sherlock RL, Shannon A, Hebel M, Lindsay D, Madsen J, Sandeman H, Hrabi B, Mortensen JK, Tosdal RM, Friedman R (2012) Volcanic stratigraphy, geochronology, and gold deposits of the Archean Hope Bay greenstone belt, Nunavut, Canada. Econ Geol 107(5):991–1042. https://doi.org/10.2113/econgeo.107.5.991
- Sibson RH (1981) Fluid flow accompanying faulting: field evidence and models. In: Simpson DW, Richards PG (ed) Earthquake prediction: An international review: American Geophysical Union, Maurice Ewing Series, v. 4, pp 593–603. https://doi.org/10.1029/ME004p0593

- Sibson RH, Robert F, Poulsen KH (1988) High-angle reverse faults, fluid-pressure cycling, and mesothermal gold-quartz deposits. Geology 16:551–555. https://doi.org/10.1130/0091-7613(1988) 016%3C0551:HARFFP%3E2.3.CO;2
- Sibson RH, Scott J (1998) Stress/fault controls on the containment and release of overpressured fluids: examples from gold-quartz vein systems in Juneau, Alaska; Victoria, Australia and Otago, New Zealand. Ore Geol Rev 13:293–306. https://doi.org/10.1016/S0169-1368(97)00023-1
- Sugiono D, Thébaud N, LaFlamme C, Fiorentini M, Laure M, Rogers J, Lorusso G, McFarlane C (2021) Integration of multiple sulfur isotopes with structural analysis unveils the evolution of ore fluids and source of sulfur at the Kanowna Belle Archean orogenic gold deposit, Yilgarn Craton, Western Australia. Miner Deposita 1–20. https://doi.org/10.1007/s00126-020-01032-1
- Sugiono D, LaFlamme C, Thébaud N, Martin L, Savard D, Fiorentini M (2022) Fault-induced gold saturation of a single auriferous fluid is a key process for orogenic gold deposit formation. Econ Geol 117(6):1405–1414. https://doi.org/10.5382/econgeo.4923
- Thurston PC, Ayer JA, Goutier J, Hamilton MA (2008) Depositional gaps in the Abitibi greenstone belt stratigraphy: A key to exploration for syngenetic mineralization. Econ Geol 103:1097–1134. https://doi.org/10.2113/gsecongeo.103.6.1097
- Tomkins AG (2013) On the source of orogenic gold. Geology 41(12):1255–1256. https://doi.org/10.1130/focus122013.1
- Tooth B, Brugger J, Ciobanu C, Liu W (2008) Modeling of gold scavenging by bismuth melts coexisting with hydrothermal fluids. Geology 36(10):815–818. https://doi.org/10.1130/G25093A.1
- Tooth B, Ciobanu CL, Green L, O'Neill B, Brugger J (2011) Bi-melt formation and gold scavenging from hydrothermal fluids: an experimental study. Geochim Cosmochim Acta 75:5423–5443. https://doi.org/10.1016/j.gca.2011.07.020
- Uemoto T, Ridley J, Mikucki E, Groves DI (2002) Fluid chemical evolution as a factor in controlling the distribution of gold at the Archean Golden Crown lode gold deposit, Murchison Province, Western Australia. Econ Geol 97:1227–1248. https://doi.org/10.2113/gsecongeo.97.6.1227
- Ward J, Mavrogenes J, Murray A, Holden P (2017) Trace element and sulfur isotopic evidence for redox changes during formation of the Wallaby Gold Deposit, Western Australia. Ore Geol Rev 82:31–48. https://doi.org/10.1016/j.oregeorev.2016.11.011
- Weatherley D, Henley RW (2013) Flash vaporisation during earth-quakes evidenced by gold deposits. Nat Geosci 6:294–298. https://doi.org/10.1038/ngeo1759
- Whitehouse MJ (2013) Multiple sulfur isotope determination by SIMS: Evaluation of reference sulfides for  $\Delta^{33}$ S with observations and a case study on the determination of  $\Delta^{36}$ S. Geostand Geoanal Res 37(1):19–33. https://doi.org/10.1111/j.1751-908X.2012.00188.x
- Wilkinson JJ, Johnston JD (1996) Pressure fluctuations, phase separation, and gold precipitation during seismic fracture propagation. Geology 24:395–398. https://doi.org/10.1130/0091-7613(1996) 024%3C0395:PFPSAG%3E2.3.CO;2
- Wilkinson L, Cruden AR, Krogh TE (1999) Timing and kinematics of post-timiskaming deformation within the larder Lake-Cadillac deformation zone, Southwest Abitibi greenstone belt, Ontario, Canada. Can J Earth Sci 36:627–647. https://doi.org/10.1139/ e99-015
- Williams-Jones AE, Heinrich CA (2005) Vapor transport of metals and the formation of magmatic-hydrothermal ore deposits. Econ Geol 100:1287–1312. https://doi.org/10.2113/gsecongeo.100.7.1287
- Wilson SA, Ridley WI, Koenig AE (2002) Development of sulfide calibration standards for the laser ablation inductively-coupled plasma mass spectrometry technique. J Anal At Spectrom 17(4):406–409. https://doi.org/10.1039/B108787H



- Woodhead JD, Hellstrom J, Hergt JM, Greig A, Maas R (2007) Isotopic and elemental imaging of geological materials by laser ablation inductively coupled plasma-mass spectrometry. Geost Geoanaly Res 31(4):331–343. https://doi.org/10.1111/j.1751-908X.2007.00104.x
- Wong L, Davis DW, Krogh TE, Robert F (1991) UPb zircon and rutile chronology of archean greenstone formation and gold mineralization in the val-d'or region, Quebec. Earth and Planet Sci Lett 104:325–336. https://doi.org/10.1016/0012-821X(91)90213-2
- Wu Y-F, Evans K, Li J-W, Fougerouse D, Large RR, Guagliardo P (2019) Metal remobilization and ore-fluid perturbation during episodic replacement of auriferous pyrite from an epizonal orogenic gold deposit. Geochim Cosmochim Acta 245:98–117. https://doi.org/10.1016/j.gca.2018.10.031
- Wu Y-F, Evans K, Hu S-Y, Fougerouse D, Zhou M-F, Fisher LA, Guagliardo P, Lei J-W (2021) Decoupling of Au and As during rapid

- pyrite crystallization. Geology 49:827–831. https://doi.org/10.1130/G48443.1
- Zhang X, Spry PG (1994) Calculated stability of aqueous tellurium species, calaverite, and hessite at elevated temperatures. Econ Geol 89:1152–1166. https://doi.org/10.2113/gsecongeo.89.5.

**Publisher's Note** Springer Nature remains neutral with regard to jurisdictional claims in published maps and institutional affiliations.

Springer Nature or its licensor (e.g. a society or other partner) holds exclusive rights to this article under a publishing agreement with the author(s) or other rightsholder(s); author self-archiving of the accepted manuscript version of this article is solely governed by the terms of such publishing agreement and applicable law.

